



Deposited via The University of Leeds.

White Rose Research Online URL for this paper:

<https://eprints.whiterose.ac.uk/id/eprint/123138/>

Version: Accepted Version

---

**Article:**

Yamasaki, T, Kobayashi, T, Wright, TJ et al. (2018) Viscoelastic crustal deformation by magmatic intrusion: A case study in the Kutcharo caldera, eastern Hokkaido, Japan. *Journal of Volcanology and Geothermal Research*, 349. pp. 128-145. ISSN: 0377-0273

<https://doi.org/10.1016/j.jvolgeores.2017.10.011>

---

(c) 2017 Elsevier B.V. This manuscript version is made available under the CC-BY-NC-ND 4.0 license <http://creativecommons.org/licenses/by-nc-nd/4.0/>

**Reuse**

This article is distributed under the terms of the Creative Commons Attribution-NonCommercial-NoDerivs (CC BY-NC-ND) licence. This licence only allows you to download this work and share it with others as long as you credit the authors, but you can't change the article in any way or use it commercially. More information and the full terms of the licence here: <https://creativecommons.org/licenses/>

**Takedown**

If you consider content in White Rose Research Online to be in breach of UK law, please notify us by emailing [eprints@whiterose.ac.uk](mailto:eprints@whiterose.ac.uk) including the URL of the record and the reason for the withdrawal request.

## Accepted Manuscript

Viscoelastic crustal deformation by magmatic intrusion: A case study in the Kutcharo caldera, eastern Hokkaido, Japan

Tadashi Yamasaki, Tomokazu Kobayashi, Tim J. Wright, Yukitoshi Fukahata



PII: S0377-0273(17)30493-6  
DOI: doi:[10.1016/j.jvolgeores.2017.10.011](https://doi.org/10.1016/j.jvolgeores.2017.10.011)  
Reference: VOLGEO 6219

To appear in: *Journal of Volcanology and Geothermal Research*

Received date: 9 August 2017  
Revised date: 17 October 2017  
Accepted date: 17 October 2017

Please cite this article as: Tadashi Yamasaki, Tomokazu Kobayashi, Tim J. Wright, Yukitoshi Fukahata, Viscoelastic crustal deformation by magmatic intrusion: A case study in the Kutcharo caldera, eastern Hokkaido, Japan. The address for the corresponding author was captured as affiliation for all authors. Please check if appropriate. *Volgeo*(2017), doi:[10.1016/j.jvolgeores.2017.10.011](https://doi.org/10.1016/j.jvolgeores.2017.10.011)

This is a PDF file of an unedited manuscript that has been accepted for publication. As a service to our customers we are providing this early version of the manuscript. The manuscript will undergo copyediting, typesetting, and review of the resulting proof before it is published in its final form. Please note that during the production process errors may be discovered which could affect the content, and all legal disclaimers that apply to the journal pertain.

**Viscoelastic crustal deformation by magmatic intrusion: a case study in the Kutcharo caldera, eastern Hokkaido, Japan**

Tadashi Yamasaki<sup>[1]\*</sup>, Tomokazu Kobayashi<sup>[2]</sup>, Tim J. Wright<sup>[3]</sup>, and Yukitoshi Fukahata<sup>[4]</sup>

<sup>[1]</sup>Geological Survey of Japan, AIST, 1-1-1 Higashi, Tsukuba, Ibaraki 305-8567, Japan

<sup>[2]</sup>Geospatial Information Authority of Japan, 1 Kitasato, Tsukuba, Ibaraki 305-0811, Japan

<sup>[3]</sup>COMET, School of Earth and Environment, University of Leeds, Leeds, LS2 9JT, United Kingdom

<sup>[4]</sup>Disaster Prevention Research Institute, Kyoto University, Uji, Kyoto 611-0011, Japan

\* All correspondence concerning this paper should be addressed to

Tadashi Yamasaki

Geological Survey of Japan, AIST

1-1-1 Higashi, Tsukuba, Ibaraki 305-8567, Japan

Phone: +81-(0)29-861-3697

Fax: +81-(0)29-856-8725

Email: [tadashi.yamasaki@aist.go.jp](mailto:tadashi.yamasaki@aist.go.jp)

**Highlights**

- The linear Maxwell viscoelastic response to the inflation of a sill is examined.
- Inflation-induced surface uplift is reduced by viscoelastic relaxation.
- Subsidence occurs after magmatic inflation stops.
- The subsidence in the Kutcharo caldera is explained by viscoelastic relaxation.
- A crustal viscosity of  $\sim 4 \times 10^{17}$  Pa s is estimated beneath the caldera.

ACCEPTED MANUSCRIPT

**ABSTRACT**

Geodetic signals observed at volcanoes, particularly their temporal patterns, have required us to make the correlation between the surface displacement and magmatic process at depth in terms of viscoelastic crustal rheology. Here we use a parallelized 3-D finite element model to examine the response of the linear Maxwell viscoelastic crust and mantle to the inflation of a sill in order to show the characteristics of a long-term volcano deformation. In the model, an oblate-spheroidal sill is instantaneously or gradually inflated in a two-layered medium that consists of an elastic layer underlain by a viscoelastic layer. Our numerical experiments show that syn-inflation surface uplift is followed by post-inflation surface subsidence as the viscoelastic substrate relaxes. For gradual inflation events, the magnitude of inflation-induced uplift is reduced by the relaxation, through which the volume of a magma inferred by matching the prediction of an elastic model with observed surface uplift could be underestimated. For a given crustal viscosity, sill depth is the principal factor controlling subsidence caused by viscoelastic relaxation. The subsidence rate is highest when the inflation occurs at the boundary between the elastic and the viscoelastic layers. The mantle viscosity has an insignificant impact unless the depth of the inflation is greater than a half the crustal thickness. We apply the viscoelastic model to the interferometric synthetic aperture radar (InSAR) data in the Kutcharo caldera, eastern Hokkaido, Japan, where the surface has slowly subsided over a period of approximately three years following about a two-year period of inflation. The emplacement of a magmatic sill is constrained to occur at a depth of  $\sim 4.5$  km, which is significantly shallower than the geophysically imaged large-scale magma chamber. The geodetically detected deformation in the caldera reflects the small-scale emplacement of a magma that ascended from the deeper chamber, but not the inflation of the chamber itself. The observed ground displacement is controlled by a lower-crustal viscosity of  $\sim 4 \times 10^{17}$  Pa s, which is lower than that inferred from some studies of post-seismic deformation, perhaps due to higher temperatures beneath the active caldera. Our results suggest that geodetic signals observed during and following magmatic intrusions need to be revisited.

**Keywords:** volcano deformation; viscoelasticity; magma intrusion; viscosity of the crust; Kutcharo caldera; geodetic data

## 1. Introduction

Modern satellite geodesy such as interferometric synthetic aperture radar (InSAR) and the Global Navigation Satellite System (GNSS) has been used to measure the dense spatiotemporal displacement of the Earth's surface (e.g. Hager et al., 1991; Seeber, 1993; Massonnet and Feigl, 1998; Pinel et al. 2014). Such analysis provides an excellent opportunity to study the mechanism of crustal deformation. Quantitative modelling study is now required to predict the characteristic pattern of surface displacement for a given particular deformation source. The geodetic observation is then able to correlate with the source (e.g. Dvorak and Dzurisin, 1997; Dzurisin, 2007; Segall, 2010). However, the correlation is not straightforward if the rheology of the crust is not simply elastic. This study takes a magmatic intrusion at depth as the source to understand how the pattern of long-term volcano deformation is characterised as a first-order approximation. For this purpose, the response of the linear Maxwell viscoelastic crust and mantle to the intrusion is particularly taken into account.

The viscoelastic relaxation of the crust and mantle has been widely recognised as one of the most important mechanisms to cause crustal deformation in a variety of spatiotemporal scales (e.g. Savage and Prescott, 1978; Stephenson, 1984; Nakada and Lambeck, 1989; Mound and Mitrovica, 1998; Jonson and Segall, 2004; Bürgmann and Dresen, 2008). The viscoelasticity is usually modelled by series and/or parallel connections of spring and dashpot, respectively, representing the instantaneous elastic and the subsequent transient viscous responses to imposed loading or unloading (e.g. Ranalli, 1995; Jaeger et al., 2007; Turcotte and Schubert, 2014). The time constant according to which the model behaviour evolves is termed the relaxation or the retardation time, both of which are usually defined by  $\eta/\mu$ , where  $\eta$  is the dashpot viscosity and  $\mu$  is the elastic spring rigidity. The viscoelastic response is non-negligible for the crustal deformation in the volcanic regions beneath which the crustal viscosity is likely lowered by a higher geothermal gradient.

The viscoelasticity predicts transient ground displacement even if a given source mechanism, whether a given displacement or pressure condition on the wall of a magma chamber or intrusion, is constant with time. The viscoelastic volcano deformation model is therefore essentially distinguishable from the elastic (e.g. Mogi, 1958; Davis et al., 1974; Dieterich and Decker, 1975; Okada, 1985; McTigue, 1987; Yang et al., 1988; Roth, 1993; Fialko et al., 2001) and elasto-plastic (e.g. Trasatti et al., 2005; Currenti et al., 2010) models. However, the transient behaviour has shown dependency on the boundary

condition of a magmatic source. For an elastically imposed-displacement source, the initial instantaneous response distributes elastic stresses into a viscoelastic medium, and the stresses are subsequently relaxed by means of viscoelasticity (e.g. Rundle, 1978; Bonafede et al., 1986; Hofton and Foulger, 1996ab; Fukahata and Matsu'ura, 2006; Hashima et al., 2014). The same process should appear for a constant pressure source embedded in a viscoelastic medium. For this type of magmatic source, however, it is also expected that the viscoelastic host rock exerts viscous deformation in response to the given pressure itself (e.g. Bonafede et al., 1986). In such case, the thermal effect of a magmatic source on the host rock would enhance the viscous response (Dragoni and Magnanensi, 1989; Newman et al., 2001; Newman et al., 2006; Del Negro et al., 2009; Gregg et al., 2013; de Silva and Gregg, 2014; Parks et al., 2015), and a compressible magma would further complicate the response (Segall, 2016).

The pressure condition would appropriately represent the mechanical boundary condition on the interface between a magma and host rock (e.g. Segall, 2010). The displacement condition is merely an assumption under which a volcano deformation model is reasonably simplified. However, models with the displacement condition have successfully explained the geodetic data of ground displacement caused by magmatic intrusion (e.g. Foulger et al., 1992; Hofton and Foulger, 1996ab; de Zeeuw-van Dal'sen et al., 2004; Nooner et al., 2009; Hamling et al., 2014). The displacement condition may be justified if the magma is newly intruded into an elastic layer underlain by a viscoelastic layer. Indeed, for magma embedded in the elastic layer, the pressure is constant with time if the further input of the mass of magma is zero (e.g. Mastin et al., 2008; Segall, 2016). The stress relaxation in the underlain viscoelastic layer may unavoidably disturb the balance between the magma pressure and the elastic host rock, but the balance may not be disturbed significantly if the size of the intrusion is small. In addition, the elastic stresses distributed into the viscoelastic layer by imposed-displacement would promptly relax, compared with a time scale over which the heat of an intruded magma weakens the surrounding rock to cause viscous deformation.

The transient viscoelastic response to a magmatic source has also shown the dependency of ground displacement on whether an elastic layer is present in the uppermost crust. Rundle (1978) showed that for a given instantaneous inflation of a spherical source embedded in an elastic layer underlain by a linear viscoelastic half-space, the initial elastic response causes the surface to uplift, but the subsequent viscoelastic relaxation abates the uplift with time. Bonafede et al. (1986) gave a similar inflation but in

homogeneous viscoelastic half-space, which, contrary to Rundle (1978), predicted that the post-inflation viscoelastic relaxation enhances the initial elastic uplift with time. The findings in these studies are significant; however, the Earth's crust likely has a depth-dependent viscosity structure (e.g. Ranalli, 1995; Stüwe, 2002; Turcotte and Shubert, 2014) in which at least to some extent the crust has a high viscosity layer that effectively acts as an elastic layer. The absence of an elastic layer should therefore be precluded in a volcano deformation model.

The behaviours of viscoelastic volcano deformation have been described in various settings of numerical and analytical models. To more systematically explain observed volcano deformation, however, it remains necessary to explore the further potential of viscoelasticity. In the present study, we focus on characteristic geodetic observation in several volcanic regions where surface uplift suddenly switches to subsidence with no significant eruptive activity, such the Kutcharo caldera in Japan (Fujiwara et al., 2017), the Yellowstone caldera in the United States (e.g. Dzurisin and Yamashita, 1987), the Campi Flegrei caldera in Italy (e.g. Bianchi et al., 1987; Dvorak and Berrino, 1991), the Asama volcano in Japan (e.g. Aoki et al., 2013), and the Aluto volcano in Ethiopia (e.g. Biggs et al., 2011; Hutchison et al., 2016). Although the subsidence in these cases has generally been interpreted in terms of migration of magma or groundwater (e.g. Dzurisin et al., 1994; Chang et al., 2007; Battaglia et al., 2006), gravity measurement has not always supported such a deficit of mass (e.g. Arnet et al., 1997). Therefore, an alternative interpretation must be proposed. The clue is found in the prediction of Rundle (1978) that inflation-induced uplift is abated by subsequent viscoelastic relaxation.

In this study, using a 3-D finite element model that consists of an elastic upper crust underlain by viscoelastic lower crust and mantle, we solve the linear Maxwell viscoelastic response to the inflation of a magmatic sill. The imposed-displacement condition is assumed to give an instantaneous or a continued inflation in either the elastic or viscoelastic layer. Intrusion given by an imposed-displacement in the viscoelastic layer would be inappropriate because a significant viscous response to the magma pressure is expected, but it can be examined how the response in the presence of an elastic layer differs from that reported by Bonafede et al. (1986).

Our numerical experiment attempts to characterise a first-ordered behaviour of the viscoelastic crust and mantle in response to the inflation. The temporal patterns of ground displacement, particularly their vertical component, are described depending on the model parameters that govern an instantaneous or gradual inflation and the rheological layering,

including elastic thickness and spatially invariable viscosities of the lower crust and mantle. The characteristic model behaviour is then applied to the ground displacement observed in the Kutcharo caldera, eastern Hokkaido, Japan (Fig. 1), to constrain the sill inflation and the crustal viscosity beneath the caldera. This study provides an important implication for the correlation of magmatic intrusion at depth and geodetically observable ground displacement in the volcanic region.

## 2. Deformation of the Kutcharo caldera, eastern Hokkaido

The Kutcharo caldera, located in eastern Hokkaido, Japan (Fig. 1a), has horizontal dimensions of 26 km (east-west) by 20 km (north-south) and is thought to be the largest caldera in Japan. The borehole and gravity studies have revealed the presence of subsurface ring fractures that give a clear image of a collapsed depression along the caldera rim (e.g. Yahata, 1989). The caldera formed along with eight explosive eruptions between  $\sim 400 \pm 100$  ka and  $\sim 40 \pm 1$  ka (e.g. Katsui and Satoh, 1963; Hirose and Nakagawa, 1995; Goto et al., 2000; Hasegawa et al., 2011), during which time the activity peaked in  $\sim 115$ -120 ka (e.g. Machida and Arai, 2003) with an erupted volume of  $\sim 175$  km<sup>3</sup> (Hasegawa et al., 2012; Hasegawa et al., 2016); this erupted volume has not been corrected to dense rock equivalent (DRE). The post-caldera period commenced at  $\sim 35$  ka, after which time Atosanupuri and Nakajima volcanoes were formed at  $\sim 30$ -20 ka (e.g. Sumita, 2003). The most recent eruption occurred at Atosanupuri volcano around 1621-1678 as a phreatic explosion (Hasegawa et al., 2017). Thus, no significant eruption has recently been detected in the caldera.

The ground displacement in and around the Kutcharo caldera has been surveyed between May 1993 and July 1998 by using the L-band synthetic aperture radar (SAR) data of the Japanese Earth Resources Satellite (JERS)-1 launched on 11 February 1992; its operation was terminated on 12 October 1998. We obtain the ground displacement data by applying an interferometric SAR (InSAR) method; essentially, the InSAR dataset analysed in Fujiwara et al. (2017) is used in this study. The analysed line-of-sight (LOS) displacement from 13 August 1993 to 21 April 1995 is depicted in Fig. 1b. The figure shows a significant LOS shortening signal consisting mainly of uplift with a peak amplitude of  $\sim 19$  cm. This deformation is  $\sim 12$ -16 km wide and is centred on at (144.410°E, 43.605°N),  $\sim 2$  km southwest of the Atosanupuri volcano.

Fig. 1c shows the LOS displacements at the centre of the deformed area, derived from each InSAR image for the time series A in Fujiwara et al. (2017) with an error of a few cm.

The volcano is expected to begin uplifting around 13 August 1993. Fujiwara et al. (2017) explained this uplift in terms of the development of a sheet-like magmatic intrusion (sill), which is strongly correlated with an increase in seismic activity. However, the uplift switches to subsidence at some time between 21 April 1995 and 7 April 1996 and then continues to subside at least until 9 June 1998 (Fig. 1c). Fujiwara et al. (2017) considered the deflation of the sill due to magmatic drain-back as the most plausible mechanism of the surface subsidence after the initial uplift event. In the present study, we explore viscoelastic relaxation as a possible alternative hypothesis with which the observed post-inflation subsidence is satisfactorily explained. For this purpose, we need to define the syn- and post-inflation periods by constructing optimal curves that best fit the observed LOS displacement data.

The two points of the data of 13 August 1993 and 21 April 1995 are linearly connected to represent the displacement history in the uplift period, assuming that no significant deformation occurred before that period. Similarly, by using the three points of the data of 7 April 1996, 25 March 1997, and 9 June 1998, an optimal curve is constructed to represent the post-inflation subsidence history. For this construction, an exponential function is adopted for the least mean squares method because the general behaviour of viscoelastic relaxation is usually exponential. The intersection between the optimal line and the curve defines the end of the syn-inflation period to be 1 May 1995, 626 days after 13 August 1993 (i.e. the syn-inflation period  $\Delta t$  is 626 days); the maximum LOS displacement is obtained to be 19.5 cm. The configuration of a sill inflation is to be constrained only from the optimal post-inflation curve, during which time the deformation is supposed to occur only by means of viscoelastic relaxation.

Another surface uplift is observed in 1998, which is also accompanied by an increase in seismic activity (Fujiwara et al., 2017; Fig. 1c). As described in the subsequent sections, however, we focus on the response of the viscoelastic crust and mantle to a single inflation event. Therefore, the data of 22 July 1998, which indicates the additional inflation event, is excluded from the present analysis.

### 3. Numerical model

A parallelised 3-D finite element code, *oregano\_ve* (e.g. Yamasaki and Houseman, 2012ab, Yamasaki et al., 2014; Yamasaki and Houseman, 2015), is used to solve the linear Maxwell viscoelastic response to the inflation of a sill in the crust. The rectangular domain has a thickness of  $Z_L'$  ( $= Z_L/L_0$ , where  $L_0$  is a reference length scale) = 10 and

covers horizontal dimensions of  $X_L' (= X_L/L_0) = 19.2$  in the  $x$ -direction and  $Y_L' (= Y_L/L_0) = 19.2$  in the  $y$ -direction (Fig. 2). The origin of the coordinate axes ( $O$ ) is placed at the centre of the modelled upper surface. The coordinate  $z$  increases downward following the right-handed system, according to which the negative and positive displacements in the  $z$ -direction indicate uplift and subsidence, respectively. For computational economy, only the domain  $x' \geq 0$  is considered as a calculation domain; the numerical code is parallelised in  $y$ -direction. The solution in the domain  $x' < 0$  is merely a copy of that in the calculation domain, which is allowed for the symmetric geometry of a sill with respect to the  $y$ - $z$  surface on  $x' = 0$ , as described below. The accuracy of the numerical code is benchmarked in Appendix A.

The top surface ( $z' = 0$ ) has zero traction in any direction. A sliding boundary condition is adopted for the remaining boundary surfaces on  $x' = 0.0$  and  $9.6$ ,  $y' = \pm 9.6$ , and  $z' = 10$ , where the normal displacement and the tangential traction are zero. Gravity is omitted from all calculations in this study to describe purely the viscoelastic response to magmatic inflation. Many previous studies have emphasised that surface topography significantly relocates the presence of a magmatic source in estimation from ground displacement (e.g. McTigue and Segall, 1988; De Natale and Pingue, 1993; De Natale et al., 1997; Williams and Wadge, 1998; Folch et al., 2000; Bonaccorso et al., 2005; Lungarini et al., 2005; Currenti et al., 2008; Bonaccorso et al., 2010; Currenti et al., 2011). However, Trasatti et al. (2003) reported that the topography causes only a minor modification of the general viscoelastic behaviour. Thus, the topographic effect is ignored in the present study to keep the model reasonably simple.

The thicknesses of the crust and mantle in the modelled domain were  $Z_c' (= Z_c/L_0) = 4$  and  $Z_m' (= Z_m/L_0) = 6$ , respectively. Then, high viscosity  $\eta_e' (= \eta_e/\eta_0$ , where  $\eta_0$  is a reference viscosity, corresponding to the spatially uniform crustal viscosity  $\eta_c) = 10^{20}$  is assigned to the uppermost crust with a thickness of  $H' (= H/L_0)$  such that it deforms effectively in an elastic fashion. The underlain viscoelastic crust and mantle have constant viscosity values of  $\eta_c' (= \eta_c/\eta_0)$  and  $\eta_m' (= \eta_m/\eta_0)$ , respectively. Although  $\eta_c'$  is held to 1, three different values of 0.1, 1, and 10 are considered for  $\eta_m'$  in order to evaluate the effect of mantle viscosity on ground displacement. Poisson's ratio  $\nu = 0.25$  and Young's modulus  $E' = E/\mu = 2(1 + \nu) = 2.5$ , where  $\mu$  is the shear modulus, are constant throughout the domain.  $4L_0$  is used to represent the thickness of the crust in this study, where  $L_0$  is 7.5 and 10 km for crustal thicknesses of 30 and 40 km, respectively.

The inflation of a sill is introduced by the split node method developed by Melosh and

Raefsky (1981). The geometry of the sill is approximated as an oblate spheroid (Fig. 3a). The sill thickness  $d'$  ( $= d/d_0$ , where  $d_0$  is a reference displacement) at the coordinate  $(x', y')$  on the surface  $z' = D'$  at time  $t'$  ( $= t/\tau_0 = \mu t/\eta_0$ , where  $\tau_0$  is the Maxwell relaxation time of the crust) is governed by

$$d'(x', y', t) = d_c'(t) [1 - (x'^2 + y'^2)/W'^2]^{1/2} \quad (1)$$

where  $d_c'(t)/2$  ( $= d_c(t)/2d_0$ ) is the polar radius, representing half the thickness at the centre of the sill,  $W'$  is the equatorial radius, representing the horizontal extent of the sill and the depth of the sill is defined by  $D'$ . In the split node method, the equivalent nodal forces are applied to obtain the opening of the sill given by Eq. (1). Because the upper and lower boundary surfaces of the modelled box have different boundary conditions, the resultant inflation is not always symmetric with respect to the equatorial plain. It is eventually no more than that the difference in depth between the upper and lower boundaries of the sill is  $d'$ . The initial volume of the sill is assumed to be zero.

The temporal change in sill thickness at the centre, i.e.  $d_c'(t)$ , is depicted in Fig. 3b. The parameter  $\Delta t'$  ( $= \Delta t/\tau_0 = \mu \Delta t/\eta_0$ ) is introduced to represent the period of sill inflation. The sill inflates either instantaneously or gradually. For the former case ( $\Delta t' = 0$ ) the inflation occurs instantaneously to have  $d_c' = d_{cp}'$  at  $t' = 0_+$  (and  $d_c' = 0$  at  $t' = 0_-$ ). For the latter case ( $\Delta t' > 0$ ),  $d_c'$  increases linearly with time to have  $d_c' = d_{cp}'$  at  $t' = \Delta t'$ . For both cases, however,  $d_c'$  is assumed to maintain a constant value of  $d_{cp}'$  for  $t' > \Delta t'$ . A dimensionless value of 100 is assigned to  $d_{cp}'$  in this study, according to which the amplitude of the calculated surface uplift is represented as a percentage of  $d_{cp}'$ .

## 4. Results

### 4.1 Model behaviour for the instantaneous inflation ( $\Delta t' = 0$ )

Fig. 4 shows the contour and profile of the surface displacement in the  $z$ -direction ( $U_z' = U_z/d_0$ ) at  $t' = 0_+$  (immediately after the instantaneous inflation), 5, 10, and 100 for the model with  $\Delta t' = 0$ , where  $H' = 1$ ,  $D' = 1$ ,  $W' = 0.5$ ,  $\eta_c' = \eta_m' = 1$ , and  $d_{cp}' = 100$  (see Appendix B for the horizontal components). At  $t' = 0_+$ , the instantaneous inflation of the sill causes the surface to uplift concentrically with respect to the axes  $x' = y' = 0$  (Fig. 4a). The minimum  $U_z'$  (i.e. the maximum uplift), with a magnitude of 20.06% of the  $d_{cp}'$ , is obtained at the centre of the uplift, i.e.  $(x', y') = (0, 0)$ , beneath which the thickness of the sill is maximum.

$|U_z|$  decreases with the distance from the centre. The arrows of  $U_{xy}' (= U_{xy}/d_0)$  at  $t' = 0_+$  radiates from the centre, showing expansion of the surface.

Then, for  $t' > 0$ , the uplift gradually abates with time through viscoelastic relaxation even though  $d_c'$  is held constant at  $d_{cp}' = 100$ . A similar behaviour was previously reported by Rundle (1978); however, spherical rather than sill-like inflation was given.  $|U_z|$  at the centre is reduced to 8.59, 4.91, and 0.80% of  $d_{cp}'$  at  $t' = 5, 10,$  and  $100$ , respectively. The concentric distribution of  $U_z'$  is maintained at all stages in the post-inflation period.  $\Delta U_{xy}'$ , which is the change in  $U_{xy}'$  accumulated since  $t' = 0_+$ , is directed radially towards the centre of the uplift, representing the surface contraction. In the profile of  $\Delta U_z'$ , the change in  $U_z'$  accumulated since  $t' = 0_+$ , a small bulge is perceived at the distance  $|y| > \sim 1.2$ . The viscoelastic relaxation causes the surface to subside at the centre of the elastic uplift but to uplift in the adjacent area.

#### 4.2 Model behaviour for the gradual inflation ( $\Delta t' > 0$ )

Fig. 5 shows the contour and profile of  $U_z'$  at  $t' = 5, 10, 50,$  and  $100$  for the model with  $\Delta t' = 10$ , where  $H' = 1, D' = 1, W' = 0.5, \eta_c' = \eta_m' = 1,$  and  $d_{cp}' = 100$ . The concentric surface uplift develops as the inflation increases linearly with time (Figs 5a and 5b).  $|U_z|$  at the centre of the uplift is 6.7 and 9.9% of  $d_{cp}'$  at  $t' = 5$  and  $10$ , respectively. The uplift is maximised at  $t' = \Delta t' = 10$ , but the magnitude is about a half the maximum uplift predicted by the model with  $\Delta t' = 0$  (Fig. 4a). The viscoelastic relaxation that occurs in the syn-inflation period reduces the surface uplift. The directions of  $U_{xy}'$  and  $\Delta U_{xy}'$ , where  $\Delta U_{xy}'$  is the change in  $U_{xy}'$  accumulated since  $t' = \Delta t'$ , show surface expansion and contraction in syn- (Figs 5a and 5b) and post-inflation (Figs 5c and 5d) periods, respectively.

The temporal  $U_z'$  at  $(x', y') = (0, 0)$  for different  $D'$  and  $\Delta t'$  are summarised in Fig. 6, where  $H' = 1, W' = 0.5, \eta_c' = \eta_m' = 1,$  and  $d_{cp}' = 100$ . For each  $D'$ ,  $U_z'$  is normalised by  $U_{z0+}'$ , where  $U_{z0+}'$  is the initial elastic uplift for the model with  $\Delta t' = 0$ ;  $U_{z0+}'$  is summarised in Table 1. This study also defines  $U_{zs}' (= U_{zs}/d_0)$  as the vertical surface displacement at  $t' = \Delta t'$  for models with  $\Delta t' \neq 0$ . Here we describe the general model behaviour only for a given  $W' = 0.5$  (see Appendix C for the dependency on  $W'$ ).

The model behaviour strongly depends on  $D'$  and  $\Delta t'$ . If the inflation occurs in the elastic layer the surface subsidence due to viscoelastic relaxation is limited. The model behaviour with  $D' = 0.2$  (Fig. 6a), in which the inflation occurs in the uppermost elastic layer, appears to be similar to that of the elastic model, being mostly independent on  $\Delta t'$ .

When, however, the inflation occurs at greater depths in the elastic layer, e.g.,  $D' = 0.5$

(Fig. 6b), the syn- and post-inflation subsidence is allowed to take place significantly.  $|U_{zs}|$  is reduced more for greater  $\Delta t'$ , and if  $\Delta t'$  is greater than  $\sim 50$  the stresses distributed by the inflation are so much relaxed at the end of the syn-inflation period that no significant surface subsidence is expected in the post-inflation period. In any case, however, the model with  $D' = 0.5$  has only the potential to reduce the surface uplift to be  $\sim 77\%$  of  $U_{z0+}'$  at the most.

On the other hand, for the models in which the sill inflation occurs in the viscoelastic layer ( $D' = 1$  and  $1.5$ ; Figs 6c and 6d), the ratio of  $U_{zs}'$  to  $U_{z0+}'$  is significantly smaller than that for the models with  $D' = 0.2$  and  $0.5$ . This indicates that the stresses are relaxed more at the end of the syn-inflation period. Nevertheless, a significant post-inflation subsidence is still available even for  $\Delta t' > \sim 50$ . Compared with the models in which the inflation occurs in the elastic layer, a greater amount of elastic stress is allowed to be relaxed. The more detailed sensitivity to  $\Delta t'$  is described in Appendix C.

#### 4.3 The post-inflation subsidence

The temporal  $U_z'$  at  $(x', y') = (0, 0)$  both in syn- and post-inflation periods has been described above for given  $H' = 1$  and  $W' = 0.5$ . Here, our focus is  $U_z'$  in the post-inflation period in more detail, where we demonstrate the dependences on  $H'$  and  $W'$ . The rate of post-inflation subsidence for the instantaneous inflation model ( $\Delta t' = 0$ ) is described in terms of the ratio of  $U_z'$  to the initial elastic uplift  $U_{z0+}'$ ; see Appendix D for the sensitivity to  $\Delta t'$ . The ratio  $U_z'/U_{z0+}'$  is plotted in Fig. 7 as a function of  $D'$  for different  $W'$  ( $= 2, 1.5, 1, 0.5,$  and  $0.1$ ) and different  $H'$  ( $= 2, 1,$  and  $0.5$ ). In general, the ratio decreases with time, showing a continuous progression of surface subsidence. However, Bonafede et al. (1986) showed that the viscoelastic response to the inflation of a magma chamber given by an imposed displacement causes the surface to continuously uplift in the absence of an elastic uppermost layer. The presence of an elastic layer plays an important role in post-inflation subsidence, where the rate at which the ratio  $U_z'/U_{z0+}'$  decreases with time is higher for greater  $H'$ . Prohibition of stress relaxation in the elastic layer is essentially required to obtain the surface subsidence by stress relaxation permitted in the viscoelastic layer.

For a given  $H'$ , the rate is strongly dependent on  $D'$ , as also shown in Fig. 7. When the inflation occurs in the elastic layer, the rate is greater for greater  $D'$ . The rate is, however, predicted to be smaller for deeper inflation when the inflation occurs in the viscoelastic layer. The highest rate is always obtained by the inflation that occurs at the interface

between the elastic and the viscoelastic layers. The models with  $D' \geq H'$  predicts simple dependence on  $W'$ , where the rate is higher for smaller  $W'$ . The models with  $D' < H'$ , however, partly complicate the dependence of the rate on  $W'$ .

#### 4.4 The effect of mantle viscosity on post-inflation subsidence

The model behaviour described above is based on the models in which the mantle viscosity  $\eta_m'$  is assumed to be the same as the crustal viscosity  $\eta_c'$ , i.e.  $\eta_m' = \eta_c' = 1$ . Here the effect of  $\eta_m'$  on the post-inflation subsidence is examined for the models with  $\Delta t' = 0$ . Fig. 8 shows the temporal  $U_z'$  normalised by the initial elastic uplift  $U_{z0+}'$ , i.e.  $U_z'/U_{z0+}'$ , for different  $\eta_m'$  of 0.1, 1, and 10, where the difference in  $U_z'/U_{z0+}'$  from that for the model with  $\eta_m' = \eta_c' = 1$  is plotted.

As intuitively understood, the rate of the post-inflation subsidence is higher for smaller  $\eta_m'$ . The effect of  $\eta_m'$ , however, is dependent on  $D'$ . A difference in  $U_z'/U_{z0+}'$  from that for the model with  $\eta_m' = \eta_c' = 1$  increases with time initially but then decreases, in which the turning point of time is later for smaller  $D'$  or greater  $\eta_m'$ . The overall temporal behaviour of the difference is not influenced by changing  $W'$ , although the difference is enhanced by increasing  $W'$ . The post-inflation subsidence is also controlled significantly by  $H'$ . The subsidence rate is higher for greater  $H'$ , and the deviation from the model with  $\eta_m' = \eta_c'$  reduces more quickly.

For models with  $D' \leq 1$ , the difference in  $U_z'/U_{z0+}'$  caused by different  $\eta_m'$  is limited to be less than  $\sim 2$ ,  $\sim 3$ , and  $\sim 7$  % of  $U_{z0+}'$  for  $W' = 0.5$ , 1, and 2, respectively. For  $D' = 2$ , however, the difference is more than 10% of  $U_{z0+}'$  for any  $W'$ . If the inflation occurs at depths deeper than the mid-crustal level, the mantle viscosity should be considered for viscoelastic volcano deformation.

## 5. Case study in the Kutcharo caldera

In this section, we apply the viscoelastic model to the geodetically observed ground displacement in the Kutcharo caldera (Fig. 1). The crustal viscosity and the configuration of the sill inflation are to be constrained according to the characteristic model behaviour such that intrusion-induced surface uplift is followed by viscoelastic surface subsidence. We aim to demonstrate the potential of viscoelastic crustal deformation to explain the surface subsidence in the Kutcharo caldera.

The seismologically constrained crustal thickness in the Kutcharo caldera region is 40 km (Katsumata, 2010; Iwasaki et al., 2013). Thus, the reference length-scale  $L_0$  is 10 km

because  $Z_c'$  (the dimensionless thickness of the crust) is set at 4 in this study. The shear modulus ( $\mu$ ) is assumed to be  $3 \times 10^{10}$  Pa, by which the Maxwell relaxation time is calculated to be  $\sim 0.1, 0.2, 0.4,$  and  $0.6$  years for  $\eta_c = 10^{17}, 2 \times 10^{17}, 4 \times 10^{17},$  and  $6 \times 10^{17}$  Pa s, respectively. Gravity is omitted in this case study too, but we have confirmed, using the semi-analytical model developed by Fukahata and Matsu'ura (2005; 2006) and Hashima et al. (2008), that the presence of the Earth's gravity ( $g = 9.8 \text{ m/s}^2$ ) does not change the results significantly for a given maximum surface uplift of  $\sim 25$  cm; the change in  $U_L$  due to the gravity is limited to be less than  $\sim 5\%$  at  $t_p = 1100$  days.

Fig. 9 shows the predicted ratio of  $U_L$  to  $U_{Ls}$  at  $t = \Delta t + t_p$ , where  $U_L$  and  $U_{Ls}$  are the LOS displacements at the centre of the uplift at  $t_p = 700$  days and 0 day, respectively, and  $\Delta t = 626$  days is the syn-inflation period. The ratios are plotted as a function of  $D$  for different  $\eta_c$ ,  $W$ , and  $H$ .  $\eta_m$  is assumed to be the same as  $\eta_c$ . The observed ratio  $U_L/U_{Ls}$  from the optimal subsidence curve is 0.527 at  $t_p = 700$  days, which is drawn by a horizontal dashed line in each panel of Fig. 9. The depth of the sill ( $D$ ) is then constrained by the intersection between the prediction and observation. The intersection is unavailable when  $\eta_c$  is  $6 \times 10^{17}$  Pa s, which is found for any thickness of the elastic layer ( $H$ ). The intersection is also available in either the elastic or viscoelastic layer for some models, but for some other models it is in both layers.

Fig. 10 summarises the value of  $D$  obtained by the intersection between the prediction and observation at different  $t_p$ . For given  $\eta_c$  and  $W$ , the intersection in the viscoelastic and elastic layer, respectively, shallows and deepens with time. This does not mean that the inflation depth changes with time; rather, the predicted subsidence is required to be greater for the later phase in order to satisfy the optimal curve. Because a stationary sill emplaced at a particular depth is considered in this study, the best-fit model for a given  $H$  is obtained by a combination of  $\eta_c$  and  $W$  with which the variation of  $D$  with  $t_p$  is minimised, and the mean value of  $D$  is taken as the best-fit value. It should be noted that the best-fit model is determined only from the models with which the intersections are available at any  $t_p$ .

In Fig. 11, the temporal LOS displacement at the centre of the uplift for the best-fit models is plotted in comparison with the observation, where the values of  $H$  are 20, 10, and 5 km. The opening of the sill ( $d_{cp}$ ) is determined as that fitting the observed uplift at the end of the syn-inflation period ( $t = \Delta t = 626$  days).  $\eta_c$  and  $W$  are constrained to be  $4\text{-}5 \times 10^{17}$  Pa s and 2 km, respectively; The viscosity may possibly be variable by a factor of  $\sim 1.5 - 2$  due to the uncertainty of  $\mu$ . The models with  $W = 1$  km are excluded from the best-

fit models because the overpressure is predicted to be an order of  $\sim 100$  MPa which is beyond the strength of the crustal rocks.  $D$ ,  $d_{cp}$ , and the volume of the sill inflation ( $\Delta V$ ) are constrained to be 19.27 km, 32.01 m, and  $0.54 \text{ km}^3$ ; 9.12 km, 7.68 m, and  $0.13 \text{ km}^3$ ; and 4.56 km, 2.16 m, and  $0.036 \text{ km}^3$  for  $H = 20, 10,$  and  $5$  km, respectively. In any case of  $H$ ,  $D$  is constrained to be slightly above the interface between the elastic and the viscoelastic layers. The change in  $U_L$  at  $t_p = 1100$  days due to the gravity effect is no more than  $\sim 0.07, \sim 3,$  and  $\sim 5\%$  for the best-fit models with  $H = 5, 10,$  and  $20$  km, respectively.

Since no data is available to describe the deformation before 13 August 1993, we cannot ignore a possibility that the inflation period might be longer than  $\Delta t = 626$  days assumed in this study. The post-inflation subsidence strongly depends on the inflation period (see Appendix D), so that the detailed analysis on the subsidence may provide some opportunity to constrain the inflation period. At the moment, however, we only have confirmed that the model behaviour is not sensitive to  $\Delta t$  significantly if the uncertainty of  $\Delta t$  is shorter than the crustal relaxation time ( $\sim 5$ -6 months for  $\eta_c = \sim 4$ - $5 \times 10^{17}$  Pa s).

The constraints on the key parameters mentioned above are derived from the geodetic data in a time range of  $0 \leq t_p \leq 700$  days, i.e., the predictions are compared with the observation in the time range from 0 to 700 days after the end of the syn-inflation period. We have also constrained the parameters from the geodetic data in two different time ranges,  $0 \leq t_p \leq 300$  days and  $0 \leq t_p \leq 1100$  days (see Table 2). The equatorial radius of the sill ( $W = 2$  km) is insensitive to the time range for any elastic thickness ( $H$ ). The crustal viscosity ( $\eta_c$ ) has only a small range of  $4$ - $5 \times 10^{17}$  Pa s. The variation of the inflation depth ( $D$ ) is limited to be less than 1.4 km. Thus, the model with the key parameters constrained only from the earliest post-inflation deformation can sufficiently well predict the later deformation.

This study has also confirmed that the best-fit models predict the displacement changes at  $t_p = \sim 13$ -15 years to be  $\sim 0.1$  cm/year for any value of  $H$ . This is inconsistent with the observation of Advanced Land Observing Satellite (ALOS)-1 operation reported by Fujiwara et al. (2017), in which significant surface subsidence with a magnitude of  $\sim 2$  cm/year is detected between 10 May 2008 and 1 October 2010. The viscoelastic relaxation associated with the inflation event that occurred in 1993-1995 has no influence on the ground subsidence from 2008 to 2010. The additional inflation events that occurred in 1998 (Fig. 1c) and later may solve the inconsistency.

The elastic model prediction (dashed blue lines in Fig. 11) is obtained by adopting the best-fit configuration of the sill inflation constrained by the viscoelastic model. The uplift at  $t$

$= \Delta t$  for the elastic model is greater than that predicted by the best-fit viscoelastic model because no viscoelastic relaxation is permitted in the elastic model. The volume change of the sill is required to be  $\sim 1.37$ - $1.41$  times less than that for the viscoelastic models in order to satisfy the observed amplitude of the uplift. However, the elastic model obviously cannot explain the post-inflation subsidence without considering the deflation of the sill.

For each case of the assumed  $H$ , the temporal profile of the predicted post-inflation LOS displacement is also plotted in Fig. 11 as a function of a distance from the centre of the uplift. The observed half-wavelength, which is the distance from the centre of the uplift to the point at which the displacement becomes zero, is  $\sim 6$ - $8$  km (Fig. 1b), as indicated by the vertical dashed line in each panel of the figure. The range of ground displacement (less than  $\sim \pm 2$ - $3$  cm) only above which the precise InSAR data are available is indicated by a shaded area. If such a limitation is considered, the half-wavelength of the uplift is predicted to be  $\sim 26$ ,  $\sim 13$ , and  $\sim 7$  km for  $H = 20$ ,  $10$ , and  $5$  km, respectively. The models with  $H = 20$  and  $10$  km should therefore be excluded; only that with  $H = 5$  km remains as the best-fit model.

The best-fit viscoelastic model has shown that the elastic model underestimates the volume of magmatic inflation by a factor of  $1.41$  (Fig. 11). Fujiwara et al. (2017) applied an elastic model to the observed surface uplift and constrained the depth and volume of the sill to be  $6$  km and  $0.022$  km<sup>3</sup>, respectively. The sill depth in Fujiwara et al. (2017) is slightly greater than that constrained in this study. In addition, the geometry of the sill in Fujiwara et al. (2017) is a rectangular with a horizontal dimension of  $8.4$  km  $\times$   $1.9$  km, being different from the spheroid assumed in this study. It is, however, interesting to note that the elastic model of Fujiwara et al. (2017) underestimates the volume of magmatic inflation by a factor close to that predicted by the viscoelastic model in this study.

## 6. Discussion

The numerical experiments in this study have predicted that ground displacement behaves in a variety of ways depending on the spatiotemporal development of the sill inflation and the rheological layering of the crust and mantle. This tells us that it is sufficiently possible to detect a magmatic intrusion at depth on the basis of geodetically observable ground displacement. The general model behaviour has characterised a first-ordered viscoelastic volcano deformation due to magmatic intrusion in such a way that the surface uplifts according to the inflation of a sill, but once the inflation stops, the surface begins to subside. The surface subsidence caused by viscoelastic relaxation, which can

occur in both syn- and post-inflation periods, is greater if the sill is inflated deeper and shallower in the elastic and viscoelastic layer, respectively. The subsidence rate is maximised by the inflation at the interface between the elastic and viscoelastic layers. Its time scale, implied in this study by the instantaneous inflation model, is such that the initial elastic uplift is reduced to a few percentage points of the sill thickness at ~50-100 times the crustal relaxation time.

Inflation-induced surface uplift has also been predicted by elastic models in many previous studies (e.g. Mogi, 1958). The present study, however, has shown that the gradual inflation of a magmatic sill is always accompanied by surface subsidence caused by viscoelastic relaxation and that accordingly, the available surface uplift is smaller than that predicted by the elastic model. In the Aira caldera, southern Kyushu, Japan, for example, the region in and around the Sakurajima volcano has continuously uplifted since the 1914 explosive eruption (e.g. Sassa, 1956; Eto et al., 1997; Iguchi et al., 2008; Iguchi, 2013). Elastic models have been adopted to estimate the volume of magma that has accumulated since the 1914 eruption from the continuous surface uplift (e.g. Iguchi et al., 2008; Hickey et al., 2016). The viscoelastic model behaviour in this study, however, has shown that the application of an elastic model to the surface uplift may possibly underestimate the volume of the magma.

Once the inflation ends through a particular process, such as the suspension of the magma supply, the surface begins to subside through viscoelastic relaxation. The inflation depth is the principal rate-controlling factor of the subsidence, as is the viscosity of the crust. Other model parameters controlling the rate include the equatorial radius of the sill, the elastic layer thickness, and the duration of the inflation.

The surface subsidence in the Kutcharo caldera has been analysed in this study along with the characteristics of the post-inflation model behaviour. The results have shown that the subsidence history, preceded by inflation-induced surface uplift, can satisfactorily be explained by viscoelastic relaxation if the depth and equatorial radius of the sill are ~4.5 km and ~2 km, respectively, and the crustal viscosity is  $4 \times 10^{17}$  Pa s. The thickness of an elastic layer in the uppermost crust is constrained to be 5 km. The mantle viscosity has an insignificant effect on the constrained inflation because it has significant impact on the ground displacement only when the inflation of the sill is deeper than ~50% of the crustal thickness (see Fig. 8).

The characteristic pattern of viscoelastic volcano deformation, uplift followed by subsidence, has been observed in other active volcanoes including the Yellowstone

caldera in United States (e.g. Dzurisin and Yamashita, 1987), the Campi Flegrei caldera in Italy (e.g. Bianchi et al., 1987; Dvorak and Berrino, 1991), the Asama volcano in Japan (e.g. Aoki et al., 2013), and the Aluto volcano in Ethiopia (e.g. Biggs et al., 2011; Hutchison et al., 2016). The uplift has usually been explained by magmatic or hydrothermal intrusion (e.g. Dzurisin et al., 1994; Chang et al., 2007), which is supported by the gravity measurements showing that uplift usually correlates with negative mass change (e.g. Berrino, 1994; Arnet et al. 1997; Battaglia et al., 2006; Tizzani et al., 2009).

The subsequent subsidence has been explained by fluid migration in the Campi Flegrei caldera (Battaglia et al., 2006). In the Yellowstone caldera, however, the subsidence is not accompanied by measurable mass change; rather, de-pressurisation of a deep hydrothermal system caused by fracturing and degassing has been suggested (Arnet et al., 1997). Similarly, the observed subsidence has been discussed in relation to the discharge of volcanic gas in the Aluto (Hutchison et al., 2016) and Asama (Kazahaya et al., 2015) volcanoes. The subsidence may possibly be caused by the cooling and contraction of melt (e.g., Dzurisin and Yamashita, 1987; Sturkell and Sigmundsson, 2000; Mann and Freymueller, 2003; Poland et al., 2006; Sturkell et al., 2006; de Zeeuw-van Dalssen et al., 2013; Hamling et al., 2015). In addition to these, we here has proposed viscoelastic relaxation as a possible mechanism of the subsidence, which does not require deflation of the magmatic source; this idea is consistent with the gravity measurement in the Yellowstone caldera. The potential of viscoelastic relaxation to explain the subsidence has been shown in the case study of the Kutcharo caldera. The trade-off between the likely mechanisms should be evaluated quantitatively in future study

The crustal viscosity estimated beneath the Kutcharo caldera, i.e.  $4 \times 10^{17}$  Pa s, is lower than that implied by the post-seismic deformation, at  $\sim 10^{18}$  to  $10^{20}$  Pa s (e.g. Suito and Hirahara, 1999; Hearn et al., 2009; Ryder et al., 2007; Bürgmann and Dresen, 2008; Ryder et al., 2011; Yamasaki and Houseman, 2012b; Yamasaki et al., 2014; Ryder et al., 2014; Yamasaki and Houseman, 2015). This may be reasonable because the crustal viscosity is expected to be lowered by the presence of magma in active volcanic regions. Indeed, on the basis of previous laboratory experiments (Jaoul et al., 1984; Patterson and Luan, 1990; Luan and Patterson, 1992; Ivins, 2000), Newman et al. (2001) summarised that a highly crystallised rhyolite melt could have viscosities of  $\sim 10^{15}$  to  $10^{17}$  Pa s for a temperature of  $\sim 670$  °C and that for quartz-bearing crystalline rocks around a magma chamber could be  $\sim 10^{17}$  to  $10^{19}$  Pa s for temperatures of  $\sim 500$  to  $600$  °C.

Similar viscosity values have been estimated in other volcanic regions. The observed

displacement fields for the period 1987-1992 after the Krafla rifting episode in north Iceland required a crustal viscosity of  $\sim 0.8-1.1 \times 10^{18}$  Pa s (Hofton and Foulger, 1996ab). The crustal viscosity beneath the Hekla volcano in south Iceland was constrained to be the order of  $10^{17}$  Pa s (Grapenthin et al., 2010). The crustal deformation inferred from microgravity data in the Three Sisters Volcanic Complex, United States, indicated that the viscosity in the crust deeper than  $\sim 3$  km is  $\sim 10^{18}$  to  $5 \times 10^{19}$  Pa s (Zurek et al., 2012). The uppermost mantle viscosity was estimated to be  $10^{18-19}$  Pa s to satisfy the post-dyking deformation in Dabbahu segment, Ethiopia (Nooner et al., 2009; Hamling et al., 2014).

The crustal structure beneath the Kutcharo caldera has been imaged by magnetotelluric (MT) studies (Ichihara et al., 2009; Honda et al., 2011). The lowest resistivity domain  $< \sim 1 \Omega \text{ m}$ , extends over a depth range deeper than  $\sim 10$  km beneath the Atosanupuri volcano. This was explained by Honda et al. (2011) as representing a 100% degree of melt with temperatures higher than  $\sim 800$  °C. In this study, however, we have constrained the sill inflation to occur at a depth of  $\sim 4.5$  km which is significantly above the lowest resistivity domain that may possibly represent a large magma chamber. The emplacement of magma propagated from the chamber, rather than the inflation of the chamber itself, is thought to cause the observed ground displacement.

The subsidence caused by viscoelastic relaxation is maximised when the inflation occurs at the boundary between the elastic and the viscoelastic layers. The inflation beneath the Kutcharo caldera has been constrained to be slightly shallower than the rheological boundary, i.e.  $D = \sim 4.5$  km for  $H = 5$  km. The elastic-viscoelastic boundary may also roughly correspond to the brittle-ductile transition because the brittle layer is generally thought to be just slightly thinner than the effective elastic layer (e.g. Pollitz and Sacks, 2002; Watts and Burov, 2003; Yamasaki et al., 2008). In addition, the stress-controlled propagation of magma favours a magmatic emplacement to occur at the brittle-ductile transition (Rubin, 1993; Hogan and Gilbert, 1995; Rubin, 1995; Watanabe et al., 1999; Burov et al., 2003). Thus, in general, a magmatic intrusion may always expect a significant effect of viscoelastic relaxation.

The rheological structure assumed in this study is oversimplified, having spatially uniform viscosities in both the viscoelastic crust and mantle and elastic layer thickness. Such an assumption is, however, still reasonably simple for investigating the general behaviour of viscoelastic relaxation in volcano deformation as a first-order approximation. The spatially distributed geodetic data require re-evaluation of the sill inflation beneath the Kutcharo caldera with respect to more complex rheological structure. However, we have

not understood thus far how the spatial rheological variation in the crust can be reflected in the ground displacements at different locations in a volcanic area. For this purpose, we need to investigate the role of the rheological heterogeneity in volcano deformation, including the spatially variable elastic thickness and viscosity due to the presence of magma. This topic, however, is beyond the scope of the present study and remains as a matter to investigate in the future study.

## 7. Conclusions

In this study, by using the 3-D finite element model, we have examined the response of the linear Maxwell viscoelastic crust and mantle to inflation of a magmatic sill. The predicted ground displacement has shown a variety of temporal behaviours depending on the configuration of the sill inflation, including the depth and equatorial radius of the sill and the duration of the inflation, and the rheological structure of the crust and mantle. In general, the viscoelastic relaxation characterises volcano deformation by syn-inflation uplift and subsequent post-inflation subsidence. The subsidence rate caused by viscoelastic relaxation in the syn- and post-inflation periods is controlled mainly by the inflation depth and is maximised when the inflation occurs at the rheological boundary between the elastic and viscoelastic layers. The available maximum rate has been implied in this study by the instantaneous inflation model such that the initial elastic surface uplift decreases to be only a few percentage points of the sill thickness over a time scale of  $\sim 50$  to 100 times the crustal relaxation time.

Greater inflation of a sill produces greater surface uplift. The syn-inflation viscoelastic relaxation has, however, predicted that the available uplift is always smaller than that predicted by elastic model. This indicates that simple application of an elastic model to the observed ground uplift may possibly underestimate the volume of the magma. On the contrary, the termination of the sill inflation causes the surface to subside through viscoelastic relaxation. The subsidence rate is actually dependent not only on the inflation depth but also on various other model parameters including the equatorial radius of the sill, the elastic layer thickness, and the duration of the inflation. The mantle viscosity has an insignificant impact on the viscoelastic subsidence unless the inflation occurs at the depths deeper than  $\sim 50\%$  of the crustal thickness.

This study has successfully explained the surface subsidence in the Kutcharo caldera in terms of only post-inflation viscoelastic relaxation. The inflation of the magmatic sill has also been constrained to occur at a depth of  $\sim 4.5$  km and to have an equatorial radius of 2

km. The sill inflation, in comparison with the geophysically imaged crustal structure by a previous magnetotelluric study (Honda et al., 2011), is located above a low-resistivity domain that may represent a large-scale magma chamber. This implies that the InSAR data used in this study reflect small-scale emplacement of a magmatic sill but not inflation of the magma chamber. The subsidence rate caused by viscoelastic relaxation, which is controlled by a viscosity of  $4 \times 10^{17}$  Pa s, is higher than that of generally observed post-seismic deformation. This may reflect a relatively higher geothermal gradient caused by the presence of magma beneath the caldera.

### Acknowledgements

This study was supported by the Secretariat of the Nuclear Regulation Authority, Japan. We thank Satoshi Fujiwara for kindly providing the InSAR dataset and Greg Houseman, Masato Iguchi and Takeshi Hasegawa for stimulating discussion and suggestion. Constructive reviews by Yosuke Aoki and an anonymous reviewer significantly improved the manuscript. The calculations in this study were carried out on the computer systems of the University of Leeds (Advanced Research Computing Node 1 and 2) and of the Earthquake and Volcano Information Center of the Earthquake Research Institute (EIC), the University of Tokyo. Generic Mapping Tools (GMT; Wessel and Smith, 1998) was used to produce the figures.

### Appendix A. The benchmark of the finite element code, oregano\_ve

Here we benchmark the accuracy of the finite element code, oregano\_ve (e.g. Yamasaki and Houseman, 2012ab, Yamasaki et al., 2014; Yamasaki and Houseman, 2015), in comparison with the analytical elastic model of Okada (1992) and the semi-analytical viscoelastic model developed by Fukahata and Matsu'ura (2005; 2006) and Hashima et al. (2008). The finite element model used for this benchmark test is the same as that shown in Fig. 2, with which the viscoelastic response to the instantaneous inflation of a sill is calculated. The geometry of the sill is, however, assumed to be a square with  $W_s$  on a side, centred on the coordinate  $(x, y) = (0, 0)$ , whose four sides are parallel either to  $x$ - or  $y$ -axis. The inflation depth is defined to be  $D_s$ , and the opening is set to be 1 m. The elastic properties, the shear modulus ( $\mu$ ) and Poisson ratio ( $\nu$ ), are  $3 \times 10^{10}$  Pa and 0.25, respectively, and are constant everywhere in the modelled domain. The elastic layer thickness  $H$  is 10 km, and the viscoelastic crust and mantle have a spatially uniform viscosity of  $\eta_c = \eta_m = 10^{19}$  Pa s.

Fig. A1 shows the initial elastic displacement, in comparison with the analytical elastic solution, where the vertical ( $U_z$ ) and horizontal ( $U_y$ ) surface displacements for different values of  $W_s$  and  $D_s$  are shown as a function of the distance from the centre of the model ( $y$ ) along the line  $x = 0$ ;  $W_s = 20, 10, \text{ and } 4 \text{ km}$ , and  $D_s = 2, 5, 10, 15, \text{ and } 20 \text{ km}$ . The numerical solutions (solid lines) are consistent with the analytical solutions (circles). The finite element code, *oregano\_ve*, provides an accurate solution to the elastic response to the inflation of a sill.

Fig. A2 shows the temporal surface displacement after the inflation, in comparison with the semi-analytical viscoelastic solution, where the vertical surface displacement ( $U_z$ ) at different locations ( $y$ ) along the line  $x = 0$  is plotted as a function of time;  $W_s = 6 \text{ and } 10 \text{ km}$ , and  $D_s = 5 \text{ and } 10 \text{ km}$ . The computational viscoelastic solutions (solid lines) also correspond reasonably well with the semi-analytical solutions (circles).

### Appendix B. The horizontal components of the viscoelastic displacement in response to the instantaneous inflation

The horizontal components of the surface displacement are briefly described here. Fig. B1 shows the contour and profile of the displacement in the  $x$ - (or  $y$ -) direction,  $U_x' = U_x/d_0$  (or  $U_y' = U_y/d_0$ ), at  $t' = 0_+, 5, 10, \text{ and } 100$ , where  $H' = 1, D' = 1, W' = 0.5, \eta_c' = \eta_m' = 1$ , and  $d_{cp}' = 100$  (these model parameters are the same as those in Fig. 4). Because the geometry of the sill is axial symmetry with respect to the  $z$ -axis, the distribution of  $U_x'$  rotated clockwise at  $90^\circ$  corresponds to that of  $U_y'$ .  $U_x'$  (or  $U_y'$ ) is zero along the line  $x'$  (or  $y'$ ) = 0. The amplitude of the displacement abates with time as the viscoelastic relaxation progresses.  $|U_x'|$  (or  $|U_y'|$ ) is maximised at  $x'$  (or  $y'$ ) =  $\pm 0.6, \pm 0.6, \pm 1.0, \text{ and } \pm 3.9$  at  $t' = 0_+, 1, 10, \text{ and } 100$ , respectively, which has magnitudes of 5.6, 4.4, 0.81, and 0.0067% of  $d_{cp}' = 100$ .  $|U_x'|$  (or  $|U_y'|$ ) at each time decreases with distance from the coordinates at which the maximum displacement is obtained.

### Appendix C. Sensitivity of syn-inflation viscoelastic displacement to the inflation period ( $\Delta t$ ) and the equatorial radius of the sill ( $W$ )

Fig. C1 shows the ratio  $U_{zs}'/U_{z0+}'$  at  $(x', y') = (0, 0)$  as a function of  $\Delta t'$  for a given  $D'$  ( $= 0.2, 0.5, 1, \text{ or } 1.5$ ), where  $U_{zs}'$  is the vertical surface displacement at  $t' = \Delta t'$  for models with  $\Delta t' \neq 0$ ,  $U_{z0+}'$  is the initial elastic uplift for models with  $\Delta t' = 0$ , and  $\eta_c' = \eta_m' = 1$ . The numerical values of  $U_{zs}'/U_{z0+}'$  at  $t' = \Delta t'$  and  $U_z'/U_{z0+}'$  at  $t' = 1000$  are summarised in Table C1 and C2, respectively. For  $D' = 0.2$  (Fig. C1a), the sensitivity of  $U_{zs}'$  to  $W'$  is weak. The

difference in  $U_{zs}'$  for different  $W'$  is limited to be  $\sim 8\%$  at the most;  $U_{zs}'$  for different  $W'$  has a range of 96.96 – 99.67, 93.97 – 99.49, 93.08 – 99.45, 92.36 – 99.43, and 91.95 – 99.42% of  $U_{z0+}'$  for  $\Delta t' = 10, 50, 100, 200,$  and  $300,$  respectively (see Fig. C1a and Table C1). The models with  $\Delta t' = 0$  predicts  $U_z'$  to be 90.72 – 99.39% of  $U_{z0+}'$  at  $t' = 1000$  (see Table C2). Therefore, the viscoelastic relaxation for the model with  $D' = 0.2$  is able to subside the surface by a maximum of only  $\sim 0.6 - 9\%$  of  $|U_{z0+}'|$ .

For  $D' = 0.5$  (Fig. C1b),  $U_{zs}'$  depends significantly on  $W'$ , where the ratio  $U_{zs}'/U_{z0+}'$  is smaller for a greater  $W'$ ; however, some deviations appear when  $\Delta t' \leq 100$ . The inflation with greater  $W'$  is able to distribute more stress in the underlain viscoelastic layer, which is the driving source of the syn-inflation viscoelastic relaxation.  $U_{zs}'$  for different  $W'$  ranges 83.64 – 92.28, 70.02 – 88.07, 65.49 – 87.20, 62.29 – 86.65, and 60.71 – 86.44% of  $U_{z0+}'$  for  $\Delta t' = 10, 50, 100, 200,$  and  $300,$  respectively (Fig. C1b and Table C1).  $U_z'$  becomes to be 54.56 – 85.87 % of  $U_{z0+}'$  at  $t' = 1000$  for the model with  $\Delta t' = 0$  (see Table C2). For the models with  $D' = 0.5$ , therefore, the viscoelastic relaxation is able to reduce the surface uplift by  $\sim 14 - 45\%$  of  $|U_{z0+}'|$ .

On the contrary, when the inflation occurs in the viscoelastic layer ( $D' = 1$  and  $1.5$ ; Figs C1c and C1d and Table C1), the dependence on  $W'$  changes significantly, where the ratio  $U_{zs}'/U_{z0+}'$  is smaller for a smaller  $W'$ . For models with  $D' = 1$ ,  $U_{zs}'$  is 46.34 – 78.04, 17.15 – 45.17, 11.28 – 31.92, 7.24 – 22.18, and 5.80 – 17.36% of  $U_{z0+}'$  for  $\Delta t' = 10, 50, 100, 200,$  and  $300,$  respectively. The ratio  $U_{zs}'/U_{z0+}'$  is greater for  $D' = 1.5$ ;  $U_{zs}' = 58.20 - 81.51, 27.57 - 50.19, 19.80 - 36.60, 14.05 - 25.45,$  and  $12.17 - 20.58\%$  of  $U_{z0+}'$  for  $\Delta t' = 10, 50, 100, 200,$  and  $300,$  respectively. The models with  $\Delta t' = 0$  show that  $U_z'$  decreases to  $\sim 0.6 - 3$  and  $\sim 1 - 5\%$  of  $U_{z0+}'$  at  $t' = 1000$  for  $D' = 1$  and  $1.5,$  respectively (see Table C2). The viscoelastic relaxation can reduce the surface uplift by more than 95 % of  $|U_{z0+}'|$  if the inflation occurs in the viscoelastic layer.

#### Appendix D. Sensitivity of post-inflation viscoelastic displacement to the inflation period ( $\Delta t$ )

For the models with  $\Delta t' \neq 0$ , the rate of post-inflation subsidence is dependent on  $\Delta t'$ . Fig. D1 plots the ratio of  $U_z'$  at  $t' = \Delta t' + t_p'$  to  $U_z'$  at  $t' = \Delta t'$  (i.e.,  $U_{zs}'$ ) as a function of  $D'$ , for which  $H'$  and  $W'$  are held to be 1 and 0.5, respectively, and  $t_p'$  is 0.5, 1, 10, and 100. The post-inflation subsidence rate is slower for a greater  $\Delta t'$ . The driving force needed to cause the post-inflation subsidence is the stresses that were not relaxed during the syn-inflation period. A greater amount of stress remains in the viscoelastic layer at the end of the

inflation when the inflation period ( $\Delta t$ ) is shorter.

## References

- Aoki, Y., Takeo, M., Ohminato, T., Nagaoka, Y., Nishida, K., 2013. Magma pathway and its structural controls of Asama Volcano, Japan. Geological Society, London, Special Publications 380, p67-84, doi: 10.1144/SP380.6.
- Arnet, F., Kahle, H.-G., Klingelé, E., Smith, R.B., Meertens, C.M., Dzurisin, D., 1997. Temporal gravity and height changes of the Yellowstone caldera, 1977-1994. Geophys. Res. Lett. 24, 2741-2744.
- Battaglia, M., Troise, C., Obrizzo, F., Pingue, F., De Natale, G., 2006. Evidence for fluid migration as the source of deformation at Campi Flegrei caldera (Italy). Geophys. Res. Lett. 33, L01307, doi:10.1029/2005GL024904.
- Berrino, G., 1994. Gravity changes induced by height-mass variations at the Campi Flegrei caldera. J. Volcanol. Geotherm. Res. 61, 293-309.
- Bianchi, R., Coradini, A., Federico, C., Giberti, G., Lanciano, P., Pozzi, J.P., Sartoris, G., Scandome, R., 1987. Modeling of Surface Deformation in Volcanic Areas: The 1970-1972 and 1982-1984 Crises of Campi Flegrei, Italy. J. Geophys. Res. 92, 14,139-14,150.
- Biggs, J., Bastow, I.D., Keir, D., Lewi, E., 2011. Pulses of deformation reveal frequently recurring shallow magmatic activity beneath the Main Ethiopian Rift. Geochem. Geophys. Geosyst. 12, Q0AB10, doi:10.1029/2011GC003662.
- Bonaccorso, A., Cianetti, S., Giunchi, C., Trasatti, E., Bonafede, M., Boschi, E., 2005. Analytical and 3-D numerical modelling of Mt. Etna (Italy) volcano inflation. Geophys. J. Int. 163, 852-862.
- Bonaccorso, A., Currenti, G., Del Negro, C., Boschi, E., 2010. Dike deflection modelling for inferring magma pressure and withdrawal, with application to Etna 2001 case. Earth Planet. Sci. Lett. 293, 121-129.
- Bonafede, M., Dragoni, M., Quarení, F., 1986. Displacement and stress fields produced by a centre of dilation and by a pressure source in a viscoelastic half-space: application to the study of ground deformation and seismic activity at Campi Flegrei, Italy. Geophys. J. R. astr. Soc. 87, 455-485.
- Bürgmann, R., Dresen, G., 2008. Rheology of the lower crust and upper mantle: Evidence from rock mechanics, geodesy and field observations. Annu. Rev. Earth Planet. Sci. 36, 531-567.

- Burov, E., Jaupart, C., Guillou-Frottier, L., 2003. Ascent and emplacement of buoyant magma bodies in brittle-ductile upper crust. *J. Geophys. Res.* 108, 2177, doi:10.1029/2002JB001904.
- Chang, W.-L., Smith, R.B., Wicks, C., Farrell, J.M., Puskas, C.M., 2007. Accelerated uplift and magmatic intrusion of the Yellowstone caldera, 2004 to 2006. *Science* 318, 952-956.
- Currenti, G., Bonaccorso, A., Del Negro, C., Scandura, D., Boschi, E., 2010. Elasto-plastic modeling of volcano ground deformation. *Earth Planet. Sci. Lett.* 296, 311-318.
- Currenti, G., Del Negro, C., Ganci, G., Scandura, D., 2008. 3D numerical deformation model of the intrusive event forerunning the 2001 Etna eruption. *Phys. Earth Planet. Inter.* 168, 88-96.
- Currenti, G., Napoli, R., Del Negro, C., 2011. Toward a realistic deformation model of the 2008 magmatic intrusion at Etna from combined DInSAR and GPS observations. *Earth Planet. Sci. Lett.* 312, 22-27.
- Davis, P.M., Hastie, L. M., Stacey, F. D., 1974. Stresses within an active volcano - With particular reference to Kilauea. *Tectonophysics* 22, 355-362.
- Del Negro, C., Currenti, G., Scandura, D., 2009. Temperature-dependent viscoelastic modeling of ground deformation: Application to Etna volcano during the 1993-1997 inflation period. *Phys. Earth Planet. Inter.* 172, 299-309.
- De Natale, G., Pingue, F., 1993. Ground deformations in collapsed caldera structures. *J. Volcanol. Geotherm. Res.* 57, 19-38.
- De Natale, G., Petrazzuoli, S.M., Pingue, F., 1997. The effect of collapse structures on ground deformations in calderas. *Geophys. Res. Lett.* 24, 1555-1558.
- de Silva, S.L., Gregg, P.M., 2014. Thermomechanical feedbacks in magmatic systems: Implications for growth, longevity, and evolution of large caldera-forming magma reservoirs and their supereruptions. *J. Volcanol. Geotherm. Res.* 282, 77-91.
- de Zeeuw-van Dalen, E., Pedersen, R., Sigmundsson, F., Pagli, C., 2004. Satellite radar interferometry 1993-1999 suggests deep accumulation of magma near the crust-mantle boundary at the Krafla volcanic system, Iceland. *Geophys. Res. Lett.* 31, L13611, doi:10.1029/2004GL020059.
- de Zeeuw-van Dalen, E., Rymer, H., Sturkell, E., Pedersen, R., Hooper, A., Sigmundsson, F., Ófeigsson, B., 2013. Geodetic data shed light on ongoing caldera subsidence at Askja, Iceland. *Bull. Volcanol.* 75, 709. <https://doi.org/10.1007/s00445-013-0709-2>.

- Dieterich, J.H., Decker, R.W., 1975. Finite element modeling of surface deformation associated with volcanism. *J. Geophys. Res.* 80, 4094-4102.
- Dragoni, M., Magnanensi, C., 1989. Displacement and stress produced by a pressurized, spherical magma chamber, surrounded by a viscoelastic shell. *Phys. Earth Planet. Inter.* 56, 316-328.
- Dvorak, J.J., Berrino, G., 1991. Recent ground movement and seismic activity in Campi Flegrei, southern Italy: Episodic growth of a resurgent dome. *J. Geophys. Res.* 96, 2309-2323.
- Dvorak, J.J., Dzurisin, D., 1997. Volcano geodesy: The search for magma reservoirs and the formation of eruptive vents. *Rev. Geophys.* 35, 343-384.
- Dzurisin, D., 2007. *Volcano Deformation: New Geodetic Monitoring Techniques*. Praxis Publishing Ltd., Chichester.
- Dzurisin, D., Yamashita, K.M., 1987. Vertical surface displacements at Yellowstone Caldera, Wyoming, 1976-1986. *J. Geophys. Res.* 92, 13,753-13,766.
- Dzurisin, D., Yamashita, K.M., Kleinman, J.W., 1994. Mechanisms of crustal uplift and subsidence at the Yellowstone caldera, Wyoming. *Bull. Volcanol.* 56, 261-270.
- Eto, T., Takayama, T., Yamamoto, K., Hendrast, M., Miki, D., Sonoda, T., Matsushima, T., Uchida, K., Yakiwara, H., Wan, Y., Kimata, F., Miyazima, R., Kobayashi, K., 1997. Re-upheaval of the ground surface at the Aira caldera - December 1991 - October 1996 -. *Annals of Disaster Prevention Research Institute, Kyoto University*, 40, 49-60 (in Japanese).
- Fialko, Y., Khazan, Y., Simons, M., 2001. Deformation due to a pressurized horizontal circular crack in an elastic half-space, with applications to volcano geodesy. *Geophys. J. Int.* 146, 181-190.
- Folch, A., Fernández, J., Rundle, J.B., Martí, J., 2000. Ground deformation in a viscoelastic medium composed of a layer overlying a half-space: a comparison between point and extended sources. *Geophys. J. Int.* 140, 37-50.
- Foulger, G. R., Jahn, C.-H., Seebet, G., Einarsson P., Julian, B. R., Heki, K., 1992. Post-rifting stress relaxation at the divergent plate boundary in Northeast Iceland. *Nature* 358, 488-490.
- Fujiwara, S., Murakami, M., Nishimura, T., Tobita, M., Yarai, H., Kobayashi, T., 2017. Volcanic deformation of Atosanupuri volcanic complex in the Kussharo caldera, Japan, from 1993 to 2016 revealed by JERS-1, ALOS, and ALOS-2 radar interferometry. *Earth, Planets and Space* 69:78, doi: 10.1186/s40623-017-0662-y.

- Fukahata, Y., Matsu'ura, M., 2005. General expressions for internal deformation fields due to a dislocation source in a multilayered elastic half-space. *Geophys. J. Int.* 161, 507-521.
- Fukahata, Y., Matsu'ura, M., 2006. Quasi-static internal deformation due to a dislocation source in a multilayered elastic/viscoelastic half-space and an equivalence theorem. *Geophys. J. Int.* 166, 418-434.
- Goto, Y., Funayama, A., Gouchi, N., Itaya, T., 2000. K-Ar ages of the Akan-Shiretoko volcanic chain lying oblique to the Kurile trench: implications for the tectonic control of volcanism. *Island Arc* 9, 204-218.
- Grapenthin, R., Ófeigsson, B.G., Sigmundsson, F., Sturkell, E., Hooper, A., 2010. Pressure sources versus surface loads: Analyzing volcano deformation signal composition with an application to Hekla volcano, Iceland. *Geophys. Res. Lett.* L20310, doi:10.1029/2010GL044590.
- Gregg, P.M., de Silva, S.L., Grosfils, E.B., 2013. Thermomechanics of shallow magma chamber pressurization: Implications for the assessment of ground deformation data at active volcanoes. *Earth Planet. Sci. Lett.* 384, 100-108.
- Hager, B.H., King, R.W., Murray, M.H., 1991. Measurement of crustal deformation using the global positioning. *Annu. Rev. Earth planet. Sci.* 19, 351-382.
- Hamling, I.J., Hreinsdóttir, S., Fournier, N., 2015. The ups and downs of the TVZ: Geodetic observations of deformation around the Taupo Volcanic Zone, New Zealand, *J. Geophys. Res. Solid Earth*, 120, 4667-4679, doi:10.1002/2015JB012125.
- Hamling, I.J., Wright, T.J., Calais, E., Lewi, E., Fukahata, Y., 2014. InSAR observations of post-rifting deformation around the Dabbahu rift segment, Afar, Ethiopia. *Geophys. J. Int.* 197, 33-49.
- Hearn, E.H., McClusky, S., Ergintav, S., Reilinger, R.E., 2009. Izmit earthquake postseismic deformation and dynamics of the North Anatolian Fault Zone. *J. Geophys. Res.* 114, B08405, 10.1029/2008JB006026.
- Hasegawa, T., Matsumoto, A., Nakagawa, M., 2016. Evolution of the 120 ka caldera-forming eruption of Kutcharo volcano, eastern Hokkaido, Japan: Geologic and petrologic evidence for multiple vent systems and rapid generation of pyroclastic flow. *J. Volcanol. Geotherm. Res.* 321, 58-72.
- Hasegawa, T., Nakagawa, M., Itoh, J., Yamamoto, T., 2011. Deposition ages of Quaternary sequences in Kushiro region, eastern Hokkaido, Japan: correlations and chronology on the basis of high-resolution tephro-stratigraphy. *J. Geol. Soc. Japan.*

- 117, 686-699 (in Japanese with English abstract).
- Hasegawa, T., Nakagawa, M., Kishimoto, H., 2012. The eruption history and silicic magma systems of caldera-forming eruptions in eastern Hokkaido, Japan. *J. Mineral. Petrol. Sci.* 107, 39-43.
- Hasegawa, T., Nakagawa, M., Miyagi, I., 2017. Re-evaluation of the history of phreatic eruptions from Atosanupuri Volcano, eastern Hokkaido, Japan: Inferred from  $^{14}\text{C}$  ages, Borehole Cores of Japan Meteorological Agency. *Jour. Geol. Soc. Japan*, 123, 269-281 (in Japanese with English abstract).
- Hashima, A., Fukahata, Y., Hashimoto, C., Matsu'ura, M., 2014. Quasi-static strain and stress fields due to a moment tensor in elastic–viscoelastic layered half-space. *Pure Appl. Geophys.* 171, 1669-1693.
- Hashima, A., Takada, Y., Fukahata, Y., Matsu'ura, M., 2008. General expressions for internal deformation due to a moment tensor in an elastic/viscoelastic multilayered half-space. *Geophys. J. Int.* 175, 992-1012.
- Hickey, J., Gottsmann, J., Nakamichi, H., Iguchi, M., 2016. Thermomechanical controls on magma supply and volcanic deformation: application to Aira caldera, Japan. *Sci. Rep.* 6, 32691; doi: 10.1038/srep32691.
- Hirose, W., Nakagawa, M., 1995. K-Ar ages of the Neogene volcanic rocks from the Kutcharo caldera region, east Hokkaido, with special reference to the Quaternary volcanic history. *J. Geol. Soc. Japan.* 101, 99-102 (in Japanese with English abstract).
- Hofton, M.A., Foulger, G.R., 1996a. Postrifting anelastic deformation around the spreading plate boundary, north Iceland 1. Modeling of the 1987-1992 deformation field using a viscoelastic Earth structure. *J. Geophys. Res.* 101, 25,403-25,421.
- Hofton, M.A., Foulger, G.R., 1996b. Postrifting anelastic deformation around the spreading plate boundary, north Iceland 2. Implications of the model derived from the 1987-1992 deformation field. *J. Geophys. Res.* 101, 25,423-25,436.
- Hogan, J.P., Gilbert, M.C., 1995. The A-type Mount Scott Granite sheet: Importance of crustal magma traps. *J. Geophys. Res.* 100, 15,779-15,792.
- Honda, R., Yamaya, Y., Ichihara, H., Hase, H., Mogi, T., Yamashita, H., Ohyama, T., Uyeshima, M., Nakagawa, M., 2011. Magnetotelluric investigation around the Kutcharo caldera region. *Geophys. Bull. Hokkaido Univ., Sapporo, Japan*, No. 74, March, 45-55 (in Japanese with English abstract).
- Hutchison, W., Biggs, J., Mather, T. A., Pyle, D. M., Lewi, E., Yirgu, G., Caliro S., Chiodini,

- G., Clor, L. E., Fischer, T. P., 2016. Causes of unrest at silicic calderas in the East African Rift: New constraints from InSAR and soil-gas chemistry at Aluto volcano, Ethiopia. *Geochem. Geophys. Geosyst.* 17, 3008-3030, doi:10.1002/2016GC006395.
- Ichihara, H., Mogi, T., Hase, H., Watanabe, T., Yamaya, Y., 2009. Resistivity and density modelling in the 1938 Kutcharo earthquake source area along a large caldera boundary. *Earth Planets Space* 61, 345-356.
- Iguchi, M., 2013. Magma movement from the deep to shallow Sakurajima Volcano as revealed by geophysical observations. *Bull. Volcanol. Soc. Japan* 58, 1-18.
- Iguchi, M., Takayama, T., Yamazaki, T., Tada, M., Suzuki, A., Ueki, S., Ohta, Y., Nakao, S., 2008. Movement of magma at Sakurajima Volcano revealed by GPS observation. *Annals of Disaster Prevention Research Institute, Kyoto University*, 51, 241-246 (in Japanese).
- Ivins, E.R., 2000. Correction to Transient creep of a composite lower crust 2. A polymineralic basis for rapidly evolving postseismic deformation modes. *J. Geophys. Res.* 105, 3229-3232.
- Iwasaki, T., Levin, V., Nikulin, A., Iidaka, T., 2013. Constraints on the Moho in Japan and Kamchatka. *Tectonophysics* 609, 184-201.
- Jaeger, J.C., Cook, N.G.W., Zimmerman, R.W., 2007. *Fundamentals of rock mechanics*. 4<sup>th</sup> ed., Blackwell, Oxford.
- Jaoul, O., Tullis, J., Kronenberg, A., 1984. The effect of varying water contents on the creep behavior of Heavitree quartzite. *J. Geophys. Res.* 89, 4298-4312.
- Johnson, K. M., Segall, P., 2004. Viscoelastic earthquake cycle models with deep stress-driven creep along the San Andreas fault system. *J. Geophys. Res.* 109, 2156-2202.
- Katsui, Y., Satoh, H., 1963. Explanatory Text of the Geological Map of Japan, Scale 1:50,000, "Mokoto-yama", Hokkaido Development Agency, Sapporo, p. 42 (in Japanese with English abstract).
- Katsumata, 2010. A., Depth of the Moho discontinuity beneath the Japanese islands estimated by travelttime analysis. *Geophys. Res., Lett.* 115, B04303, doi:10.1029/2008JB005864.
- Kazahaya, R., Aoki, Y., Shinohara, H., 2015. Budget of shallow magma plumbing system at Asama Volcano, Japan, revealed by ground deformation and volcanic gas studies. *J. Geophys. Res. Solid Earth* 120, doi:10.1002/2014JB011715.
- Luan, F.C., Patterson, M.S., 1992. Preparation and deformation of synthetic aggregates of quartz. *J. Geophys. Res.* 97, 301-320.

- Lungarini, L., Troise, C., Meo, M., De Natale, G., 2005. Finite element modelling of topographic effects on elastic ground deformation at Mt. Etna. *J. Volcanol. Geotherm. Res.* 144, 257-271.
- Machida, H., Arai, F., 2003. Atlas of Tephra in and Around Japan. Tokyo University Press, Tokyo (in Japanese).
- Mann, D., Freymueller, J., 2003. Volcanic and tectonic deformation on Unimak Island in the Aleutian Arc, Alaska. *J. Geophys. Res.* 108, 2108, doi:10.1029/2002JB001925.
- Massonnet, D., Feigl, K.L., 1998. Radar interferometry and its application to changes in the earth's surface. *Rev. Geophys.* 36, 441-500.
- Mastin, L.G., Roeloffs, E., Beeler, N.M., Quick, J.E., 2008. Constraints on the size, overpressure, and volatile content of the Mount St. Helens magma system from geodetic and dome-growth measurements during the 2004-2006+ eruption. In: Sherrod, D.R., Scott, W.E. and Stauffer, P. (Eds.), *A volcano Rekindle: The renewed eruption of Mount St. Helens, 2004-2006*. U.S. Geol. Surv. Prof. Paper, 1750, 461-488.
- McTigue, D.F., 1987. Elastic stress and deformation near a finite spherical magma body: resolution of the point source paradox. *J. Geophys. Res.* 92, 12,931-12,940.
- McTigue, D.F., Segall, P., 1988. Displacements and tilts from dip-slip faults and magma chambers beneath irregular surface topography. *Geophys. Res. Lett.* 15, 601-604.
- Melosh, H.J., Raefsky, A., 1981. A simple and efficient method for introducing faults into finite element computations. *Bull. Seism. Soc. Am.* 71, 1391-1400.
- Mogi, K., 1958. Relations between eruptions of various volcanoes and the deformations of the ground surfaces around them. *Bull. Earthq. Res. Inst.* 26, 99-134.
- Mound, J.E., Mitrovica, J.X., 1998. True polar wander as a mechanism for second-order sea-level variations. *Science* 279, 534-537.
- Nakada, M., Lambeck, K., 1989. Late Pleistocene and Holocene sea-level change in the Australian region and mantle rheology. *Geophys. J. Int.* 96, 497-517.
- Newman, A.V., Dixon, T.H., Ofoegbu, G.I., Dixon, J.E., 2001. Geodetic and seismic constraints on recent activity at Long Valley Caldera, California: evidence for viscoelastic rheology. *J. Volcanol. Geotherm. Res.* 105, 183-206.
- Newman, A.V., Dixon, T.H., Gourmelen, N., 2006. A four-dimensional viscoelastic deformation model for Long Valley Caldera, California, between 1995 and 2000. *J. Volcanol. Geotherm. Res.* 150, 244-269.
- Nooner, S.L., Bennati, L., Calais, E., Buck, W. R., Hamling, I.J., Wright, T.J., Lewi E.,

2009. Post-rifting relaxation in the Afar region, Ethiopia. *Geophys. Res. Lett.* 36, L21308, doi:10.1029/2009GL040502.
- Okada, Y., 1985. Surface deformation due to shear and tensile faults in a half-space. *Bull. Seism. Soc. Am.* 75, 1135-1154.
- Parks, M.M., Moore, J.D.P., Papanikolaou, X., Biggs, J., Mather, T.A., Pyle, D.M., Raptakis, C., Paradissis, D., Hooper, A., Parsons, B., Nomikou, P., 2015. From quiescence to unrest: 20 years of satellite geodetic measurements at Santorini volcano, Greece. *J. Geophys. Res.* 120, 1309-1328, doi:10.1002/2014JB011540.
- Patterson, M.S., Luan, F.C., 1990. Quartzite rheology under geological conditions. In: Knipe, R.J., Rutter, E.H. (Eds.), *Deformation Mechanisms, Rheology and Tectonics*. Geol. Soc., London, Spec. Publ. 54, 299-307.
- Pinel, V., Poland, M.P., Hooper, A., 2014. Volcanology: Lessons learned from Synthetic Aperture Radar imagery. *J. Volcanol. Geotherm. Res.* 289, 81-113.
- Poland, M.P., Bürgmann, R., Dzurisin, D., Lisowski, M., Masterlark, T., Owen, S., Fink, J., 2006. Constraints on the mechanism of long-term, steady subsidence at Medicine Lake volcano, northern California, from GPS, leveling and InSAR. *J. Volcanol. Geotherm. Res.* 150, 55-78.
- Pollitz, F.F., Sacks, I.S., 2002. Stress triggering of the 1999 Hector Mine Earthquake by transient deformation following the 1992 Landers Earthquake. *Bull. Seism. Soc. Am.* 92, 1487-1496.
- Ranalli, G., 1995. *Rheology of the Earth*, 2nd edn, Chapman and Hall, London.
- Roth, F., 1993. Deformations in a layered crust due to a system of cracks: Modeling the effect of dike injections or dilatancy. *J. Geophys. Res.* 98, 4543-4551.
- Rubin, A.M., 1993. Dykes vs diapirs in viscoelastic rock. *Earth Planet Sci. Lett.* 117, 653-670.
- Rubin, A.M., 1995. Propagation of magma-filled cracks. *Annu. Rev. Earth Planet. Sci.* 23, 287-336.
- Rundle, J.B., 1978. Viscoelastic crustal deformation by finite quasi-static sources. *J. Geophys. Res.* 83, 5937-5945.
- Ryder, I., Bürgmann, R., Pollitz, F.F., 2011. Lower crustal relaxation beneath the Tibetan Plateau and Qaidam Basin following the 2001 Kokoxili earthquake. *Geophys. J. Int.* 187, 613-630.
- Ryder, I., Parsons, B., Wright, T.J., Funning, G.J., 2007. Post-seismic motion following the 1997 Manyi (Tibet) earthquake: InSAR observations and modelling. *Geophys. J. Int.*

169, 1009-1027.

- Ryder, I., Wang, H., Bie, L., Rietbrock, A., 2014. Geodetic imaging of late postseismic lower crustal flow in Tibet. *Earth Planet. Sci. Lett.* 404, 136-143.
- Sassa, K., 1956. A few problems on prediction of earthquake (II). Proceedings of the fifth anniversary of founding of Disaster Prevention Research Institute, Kyoto University, 3-7 (in Japanese).
- Savage, J. C., Prescott, W.H., 1978. Asthenosphere readjustment and the earthquake cycle. *J. Geophys. Res.* 83, 3369–3376.
- Seeber, G., 1993. *Satellite Geodesy: Foundations, Methods, and Applications*. Walter de Gruyter, New York.
- Segall, P., 2010. *Earthquake and volcano deformation*, Princeton University Press, New Jersey.
- Segall, P., 2016. Repressurization following eruption from a magma chamber with a viscoelastic aureole. *J. Geophys. Res. Solid Earth* 121, 8501-8522, doi: 10.1002/2016JB013597.
- Stephenson, R., 1984. Flexural models of continental lithosphere based on the long term decay of topography. *Geophys. J. R. astr. Soc.* 77, 385-413.
- Suito, H., Hirahara, K., 1999. Simulation of postseismic deformation caused by the 1896 Riku-u earthquake, northeast Japan: re-evaluation of the viscosity in the upper mantle. *Geophys. Res. Lett.* 26, 2561-2564.
- Sumita, M., 2003. Kutcharo caldera and ignimbrite. In: Koaze, T., Nogami, M., Ono, Y., Hirakawa, K. (Eds.), *Regional Geomorphology of the Japanese Islands Vol. 2*. University of Tokyo Press, Geomorphology of Hokkaido, 110-111 (in Japanese).
- Sturkell, E., Sigmundsson, F., 2000. Continuous deflation of the Askja caldera, Iceland, during the 1983-1998 noneruptive period. *J. Geophys Res.* 105, 25,671-25,684.
- Sturkell, E., Sigmundsson, F., Slunga, R., 2006. 1983-2003 decaying rate of deflation at Askja caldera: Pressure decrease in an extensive magma plumbing system at a spreading plate boundary. *Bull. Volcanol.* 68, 727-735.
- Stüwe, K., 2002. *Geodynamics of the lithosphere*. Springer, Berlin.
- Tizzani, P., Battaglia, M., Zeni, G., Atzori, S., Berardino, P., Lanari, R., 2009. Uplift and magma intrusion at Long Valley caldera from InSAR and gravity measurements. *Geology* 37, 63-66.
- Trasatti, E., Giunchi, C., Bonafede, M., 2003. Effects of topography and rheological layering on ground deformation in volcanic regions. *J. Volcanol. Geotherm. Res.* 122,

89-110.

- Trasatti, E., Giunchi, C., Bonafede, M., 2005. Structural and rheological constraints on source depth and overpressure estimates at the Campi Flegrei caldera, Italy. *J. Volcanol. Geotherm. Res.* 144, 105-118.
- Turcotte, D., Shubert, G., 2014. *Geodynamics (Third Edition)*. Cambridge University Press, Cambridge.
- Watanabe, T., Koyaguchi, T., Seno, T., 1999. Tectonic stress controls on ascent and emplacement of magmas. *J. Volcanol. Geotherm. Res.* 91, 65-78.
- Watts, A.B., Burov, E.B., 2003. Lithospheric strength and its relationship to the elastic and seismogenic layer thickness. *Earth planet. Sci. Lett.* 213, 113-131.
- Wessel, P., Smith, W.H.F., 1998. New, improved version of generic mapping tools released. *EOS Trans. AGU* 79(47), 579.
- Williams, C.A., Wadge, G., 1998. The effects of topography on magma chamber deformation models: Application to Mt. Etna and radar interferometry. *Geophys. Res. Lett.* 25, 1549-1552.
- Yahata, M., 1989. The Kutcharo Caldera - a consideration on the relationship between the basement structure and the formation of caldera. *Monogr. Assoc. Geol. Collab. Japan* 36, 191-208 (in Japanese with English abstract).
- Yamasaki, T., Houseman, G.A., 2012a. The signature of depth-dependent viscosity structure in post-seismic deformation. *Geophys. J. Int.* 190, 769-784.
- Yamasaki, T., Houseman, G.A., 2012b. The crustal viscosity gradient measured from post-seismic deformation: a case study of the 1997 Manyi (Tibet) earthquake. *Earth Planet. Sci. Lett.* 351-352, 105-114.
- Yamasaki, T., Houseman, G.A., 2015. Analysis of the spatial viscosity variation in the crust beneath the western North Anatolian Fault. *J. Geodyn.* 88, 80-89.
- Yamasaki, T., Miura, H., Nogi, Y., 2008. Numerical modelling study on the flexural uplift of the Transantarctic Mountains. *Geophys. J. Int.* 174, 377-390.
- Yamasaki, T., Wright, T.J., Houseman, G.A., 2014. Weak ductile shear zone beneath a major strike-slip fault: Inferences from earthquake cycle model constrained by geodetic observations of the western North Anatolian Fault Zone. *J. Geophys. Res.* 119, 3678-3699, doi: 10.1002/2013JB010347.
- Yang, X.M., Davis, P.M., Dieterich, J.M., 1988. Deformation from inflation of a dipping finite prolate spheroid in an elastic half-space as a model for volcanic stressing. *J. Geophys. Res.* 93, 4249-4257.

Zurek, J., William-Jones, G., Johnson, D., Eggers, A., 2012. Constraining volcanic inflation at Three Sisters Volcanic Field in Oregon, USA, through microgravity and deformation modeling. *Geochem. Geophys. Geosyst.* 13, Q10013, doi:10.1029/2012GC004341.

### Figure captions

Fig. 1: InSAR data obtained in and around the Kutcharo caldera and used in this study. The data were originally analysed in Fujiwara et al. (2017). (a) Location of the InSAR data. (b) Line-of-sight (LOS) displacement image of the area obtained from the InSAR data for the period 13 August 1993 to 21 April 1995. A significant LOS shortening signal is centred on at (144.410°E, 43.605°N), ~2 km southwest of the Atosanupuri volcano, having a peak amplitude of ~19 cm. (c) Temporal LOS displacement at the centre of the uplift, at (144.410°E, 43.605°N; open circles). The least squares method with linear and exponential functions are adopted for the data on and before 21 April 1995 and on and after 7 April 1996 excluding the datum on 22 July 1998, respectively, to obtain the optimal curve (red curve) that best represents the history of the ground displacement. The surface uplift switches to subsidence at 1 May 1995, and the subsidence continues at least until 9 June 1998.

Fig. 2: Schematic figure of the finite element model used in this study. The modelled domain, in which a sill is inflated at a particular depth level, is a rectangular with a thickness of  $Z_L' (= Z_L/L_0$ , where  $L_0$  is a reference length scale) = 10, and horizontal dimensions in the  $x$ - and  $y$ -directions of  $X_L' (= X_L/L_0) = 19.2$  and  $Y_L' (= Y_L/L_0) = 19.2$ , respectively. The right-handed coordinate system, with the axial origin ( $O$ ) at the centre of the modelled upper surface, defines uplift and subsidence by negative and positive displacements in the  $z$ -direction, respectively. Only the domain  $x' (= x/L_0) \geq 0$  is considered as a solution domain in order to reduce the computational load, for which traction in any direction is zero on the top surface ( $z' = z/L_0 = 0$ ) and normal displacement and tangential traction are zero on the boundary surfaces of  $x' = 0.0$  and  $9.6$ ,  $y' (= y/L_0) = \pm 9.6$  and  $z' = 10$ . The solution in the domain  $x' < 0$  is the same as that in  $x' \geq 0$ . The crust and mantle have thicknesses of  $Z_c' (= Z_c/L_0) = 4$  and  $Z_m' (= Z_m/L_0) = 6$ , respectively. The viscosities of the crust and mantle are spatially uniform  $\eta_c' (= \eta_c/\eta_0$ , where  $\eta_0$  is a reference viscosity) and  $\eta_m' (= \eta_m/\eta_0)$ , respectively. However, the viscosity of  $\eta_e' (= \eta_e/\eta_0)$  given to the uppermost crust with a thickness of  $H (= H/L_0)$  is sufficiently high ( $\eta_e' = 10^{20}$ ) to effectively deform elastically.

Fig. 3 Configuration of the magmatic sill assumed in this study. (a) The geometry of the spheroidal sill is defined by the depth of the equatorial plane ( $D' = D/L_0$ ), the equatorial radius ( $W' = W/L_0$ ), and the thickness at the centre of the sill ( $d_c' = d_c/d_0$ ). (b) The temporal development of  $d_c'$  assumed in this study. For  $\Delta t' (= \Delta t/\tau_0 = \mu\Delta t/\eta_0$ , where  $\tau_0$  is the Maxwell relaxation time of the crust) = 0,  $d_c'$  instantaneously becomes  $d_{cp}' (= d_{cp}/d_0)$  at  $t' = 0_+$  immediately after the inflation ( $d_c' = 0$  at  $t' = 0_-$ , immediately before the inflation), and then at  $t' > 0$  it is held to be constant at  $d_{cp}'$ . For  $\Delta t' > 0$ ,  $d_c'$  increases linearly with time, with  $d_{cp}'$  at  $t' = \Delta t'$ ;  $t' > \Delta t'$ , it is held constant at  $d_{cp}'$ .  $d_{cp}'$  is assumed to be 100 in this study.

Fig. 4: Contour and profile of the surface displacement in the  $z$ -direction  $U_z' (= U_z/d_0)$  for the model with  $\Delta t' = 0$ . The time  $t'$  ( $= t/\tau_0 = \mu t/\eta_0$ ) is (a)  $0_+$  (immediately after the instantaneous inflation), (b) 5, (c) 10, and (d) 100. Arrows in the contour at  $t' = 0_+$  show surface displacements in the  $x$ - $y$  direction ( $U_{xy}' = U_{xy}/d_0$ ); those at  $t' > 0$  the change in  $U_{xy}$  ( $\Delta U_{xy}'$ ) which has been accumulating since  $t' = 0_+$ . The profiles of  $U_z'$  and  $\Delta U_z'$  along the line  $x' = 0$  are plotted by red and blue curves, respectively, where  $\Delta U_z'$  is the change in  $U_z'$  caused by viscoelastic relaxation.  $H' = 1$ ,  $D' = 1$ ,  $W' = 0.5$ , and  $\eta_c' = \eta_m' = 1$ .

Fig. 5: Contour and profile of the vertical surface displacement  $U_z' (= U_z/d_0)$  at  $t' =$  (a) 5, (b) 10, (c) 50, and (d) 100 for  $\Delta t' = 10$ . The profile is taken along the line  $x' = 0$ . Arrows in the contour at  $t' \leq 10$  show surface displacement in the  $x$ - $y$  direction ( $U_{xy}' = U_{xy}/d_0$ ) caused by the inflation of the sill; those at  $t' > 10$  show the change in  $U_{xy}$  ( $\Delta U_{xy}'$ ), which has been accumulating since  $t' = 10$ .  $H' = 1$ ,  $D' = 1$ ,  $W' = 0.5$ , and  $\eta_c' = \eta_m' = 1$ .

Fig. 6: Temporal surface displacement in the  $z$ -direction  $U_z'$  at  $(x', y') = (0, 0)$  for models with  $D' =$  (a) 0.2, (b) 0.5, (c) 1, and (d) 1.5.  $\Delta t' =$  (blue) 0, (red) 10, (green) 50, (purple) 100, (orange) 200, and (aqua) 300.  $U_z'$  is normalised by  $U_{z0+}'$  for each case of  $D'$ , where  $U_{z0+}'$  is the initial elastic uplift for the model with  $\Delta t' = 0$ ;  $U_{z0+}' = -86.25, -50.11, -20.06, \text{ and } -10.03$  for  $D' = 0.2, 0.5, 1, \text{ and } 1.5$ , respectively.  $W' = 0.5$ , and  $\eta_c' = \eta_m' = 1$ .

Fig. 7: Post-inflation surface displacement in the  $z$ -direction  $U_z'$  at  $(x', y') = (0, 0)$  as a function of  $D'$  for models with  $\Delta t' = 0$ .  $U_z'$  is normalised by the initial elastic displacement  $U_{z0+}'$ .  $H' =$  (a), (b), (c), (d) 2; (e), (f), (g), (h) 1; and (i), (j), (k), (l) 0.5. The time  $t' =$  (a), (e), (i) 1; (b), (f), (j) 5; (c), (g), (k) 10; and (d), (h), (l) 50, and  $W' =$  (blue) 2, (red) 1.5, (green) 1,

(purple) 0.5, and (orange) 0.1.  $\eta_c' = \eta_m' = 1$ .

Fig. 8: Post-inflation surface displacement in the  $z$ -direction  $U_z'$  at  $(x', y') = (0, 0)$  as a function of  $t'$  for models with  $\Delta t' = 0$ , where  $U_z'$  is normalised by the initial elastic displacement  $U_{z0+}'$ , and the difference in  $U_z'/U_{z0+}'$  from that of the model with  $\eta_m' = \eta_c' = 1$  is plotted.  $\eta_c'$  is held to be 1.  $\eta_m' =$  (blue) 0.1, (red) 1, and (green) 10,  $D' =$  (a), (b), (c) 0.5; (d), (e), (f) 1; and (g), (h), (i) 2 and  $W' =$  (a), (d), (g) 2; (b), (e), (h) 1; and (c), (f), (i) 0.5.  $H' =$  (solid line) 1, (dashed line) 0.5, and (dotted and dashed line) 2.

Fig. 9: Post-inflation LOS displacement at the centre of the uplift plotted as a function of  $D$  for models with  $\eta_c = 10^{17}$ ,  $2 \times 10^{17}$ ,  $4 \times 10^{17}$ , and  $6 \times 10^{17}$ , where the LOS displacement ( $U_L$ ) is normalised by LOS displacement at the end of the syn-inflation period ( $U_{Ls}$ ). The time  $t_p$  is 700 days after the end of the inflation; the time  $t$  since 13 August 1993 is defined by  $t = \Delta t + t_p$ , where  $\Delta t = 626$  days is the syn-inflation period.  $\eta_m$  is assumed to be the same as  $\eta_c$ .  $H =$  (a), (b), (c), (d), 20 km; (e), (f), (g), (h) 10 km; and (i), (j), (k), (l) 5 km.  $W =$  (blue) 15 km, (red) 10 km, (green) 5 km, (purple) 2 km, (orange) 1 km. The horizontal dashed line indicates the observed ratio of LOS displacement at  $t_p = 700$  days to the displacement at  $t_p = 0$  day.

Fig. 10: Depth of the sill inflation ( $D$ ) estimated at different times ( $t_p$ ) in the post-inflation period, where  $H =$  (a) 20 km, (b) 10 km, and (c) 5 km,  $\eta_c =$  (blue)  $10^{17}$  Pa s, (red)  $2 \times 10^{17}$  Pa s, (green)  $3 \times 10^{17}$  Pa s, (purple)  $4 \times 10^{17}$  Pa s, and (orange)  $5 \times 10^{17}$  Pa s and  $W =$  (circle) 15 km, (square) 10 km, (triangle) 5 km, (diamond) 2 km, and (star) 1 km.  $\eta_m$  is assumed to be the same as  $\eta_c$ . The horizontal dashed line in each panel indicates the depth of the boundary between the elastic and the viscoelastic layers.

Fig. 11: Best-fit model predictions compared with the observation: (a), (b)  $H = 20$  km,  $\eta_c = 5 \times 10^{17}$  Pa s,  $D = 19.27$  km,  $W = 2$  km,  $d_{cp} = 32.01$  m, and  $\Delta V = 0.54$  km<sup>3</sup>; (c), (d)  $H = 10$  km,  $4 \times 10^{17}$  Pa s,  $D = 9.12$  km,  $W = 2$  km,  $d_{cp} = 7.68$  m, and  $\Delta V = 0.13$  km<sup>3</sup>; and (e), (f)  $H = 5$  km,  $4 \times 10^{17}$  Pa s,  $D = 4.56$  km,  $W = 2$  km,  $d_{cp} = 2.16$  m, and  $\Delta V = 0.036$  km<sup>3</sup>, where  $\Delta V$  is the change in the volume of the sill.  $\eta_m$  is assumed to be the same as  $\eta_c$ . (a), (c), (e) LOS displacement as a function of time, where open circles are the observed LOS displacement at the centre of the uplift, the black curve is the optimal displacement history obtained by means of least squares method, and the red curve is the best-fit-predicted

LOS displacement. The dashed blue line is the elastic model prediction with the parameters of the sill constrained by the viscoelastic model. (b), (d), (f) Predicted LOS displacement profiles at  $t_p =$  (blue) 0 day, (red) 300 days, (green) 500 days, (purple) 700 days, (orange) 900 days, and (aqua) 1100 days.

Fig. A1: Initial elastic surface displacement due to the instantaneous inflation of a rectangular sill, where the numerical (solid lines) and analytical (circles) solutions are plotted as a function of  $y$ . (a, b, c) Displacement in the  $z$ -direction  $U_z$  and (a', b', c') displacement in the  $y$ -direction  $U_y$ .  $W_s =$  (a, a') 20 km, (b, b') 10 km, and (c, c') 4 km.  $D_s =$  (blue) 2 km, (red) 5 km, (green) 10 km, (purple) 15 km, and (orange) 20 km.

Fig. A2: Viscoelastic surface displacement in the  $z$ -direction ( $U_z$ ) after the instantaneous inflation of a rectangular sill, where the numerical (solid lines) and semi-analytical (circles) solutions are plotted as a function of time.  $y =$  (a) 0 km, (b) 5 km, (c) 10 km, (d) 20 km, (e) 30 km, and (f) 50 km. (blue)  $W_r = 10$  km and  $D_r = 5$  km, (red)  $W_r = 10$  km and  $D_r = 10$  km, and (green)  $W_r = 6$  km and  $D_r = 5$  km.  $H = 10$  km, and  $\eta_c = \eta_m = 10^{19}$  Pa s.

Fig. B1: Contour and profile of the horizontal surface displacement  $U_x' (= U_x/d_0)$  or  $U_y' (= U_y/d_0)$  at  $t' =$  (a)  $0_+$  (immediately after the instantaneous inflation), (b) 5, (c) 10, and (d) 100 for the model with  $\Delta t' = 0$ . The profiles of  $U_x'$  (or  $U_y'$ ) and  $\Delta U_x'$  (or  $\Delta U_y'$ ) along the line  $y'$  (or  $x'$ ) = 0 are plotted by red and blue curves, respectively, where  $\Delta U_x'$  (or  $\Delta U_y'$ ) is the change in  $U_x'$  (or  $U_y'$ ) due to viscoelastic relaxation.  $H' = 1$ ,  $D' = 1$ ,  $W' = 0.5$ , and  $\eta_c' = \eta_m' = 1$ .

Fig. C1: Surface displacement in the  $z$ -direction at  $(x', y') = (0, 0)$  at  $t' = \Delta t'$ , i.e.  $U_{zs}'$ , as a function of  $\Delta t'$ . For each  $D'$ ,  $U_{zs}'$  is normalised by  $U_{z0+}'$ .  $D' =$  (a) 0.2, (b) 0.5, (c) 1, and (d) 1.5, and  $W' =$  (blue) 2, (red) 1.5, (green) 1, (purple) 0.5, and (orange) 0.1.  $H' = 1$ , and  $\eta_c' = \eta_m' = 1$ .

Fig. D1: Post-inflation surface displacement in the  $z$ -direction  $U_z'$  at  $(x', y') = (0, 0)$  as a function of  $D'$  for models with  $\Delta t' \geq 0$ .  $U_z'$  is normalised by the displacement at  $t' = \Delta t'$  ( $U_{zs}'$ ).  $H'$  and  $W'$  are fixed at 1 and 0.5, respectively. The time  $t'$  is  $\Delta t' + t_p'$ , where  $t_p'$  is (a) 0.5, (b) 1, (c) 10 and (d) 100.  $\Delta t' =$  (blue) 0, (red) 10, (green) 50, (purple) 100, and (orange) 200.  $\eta_c' = \eta_m' = 1$ .

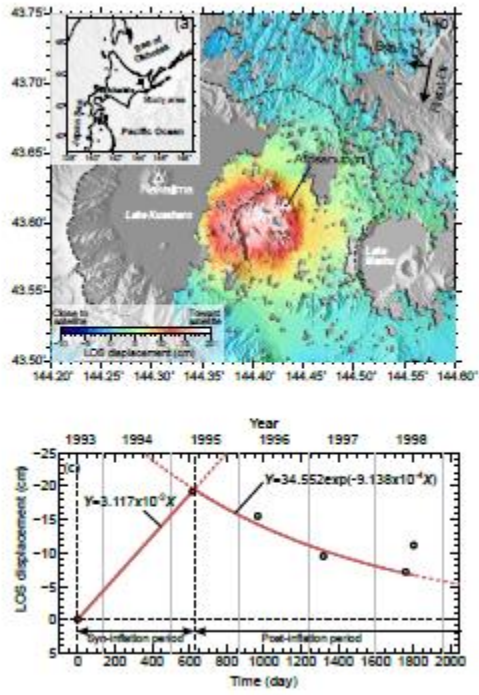


Fig. 1

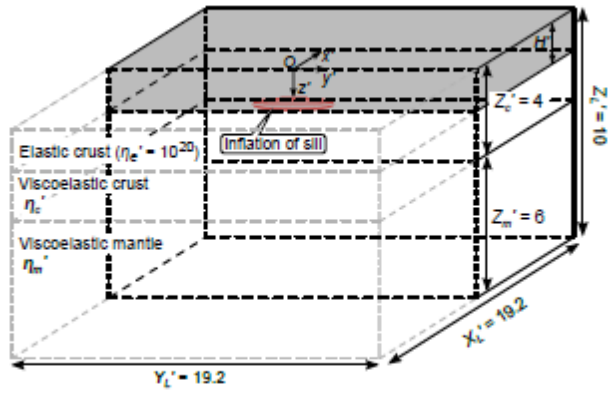


Fig. 2

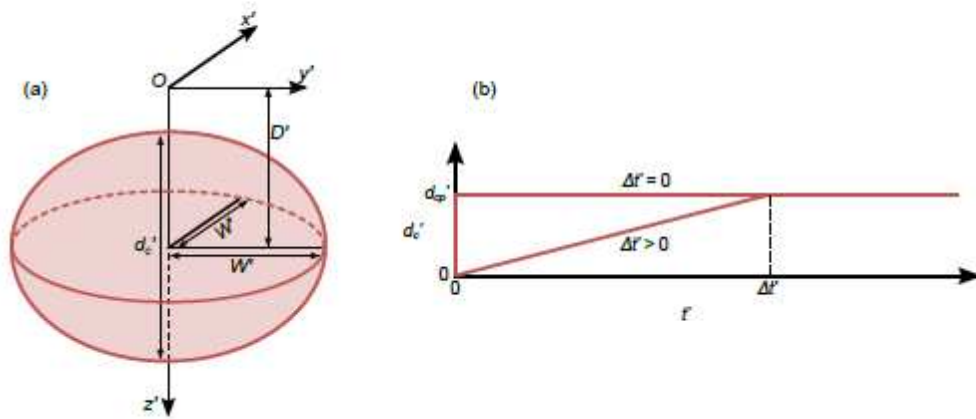


Fig. 3

ACCEPTED MANUSCRIPT

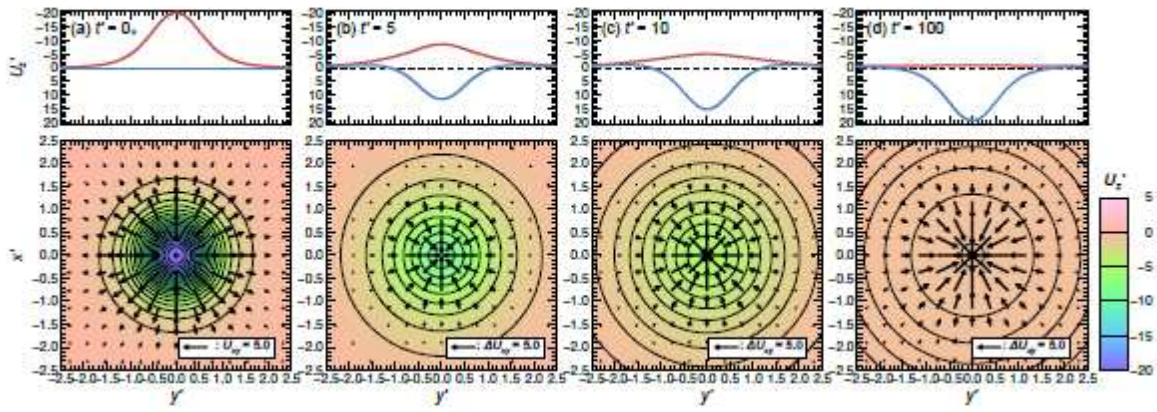


Fig. 4

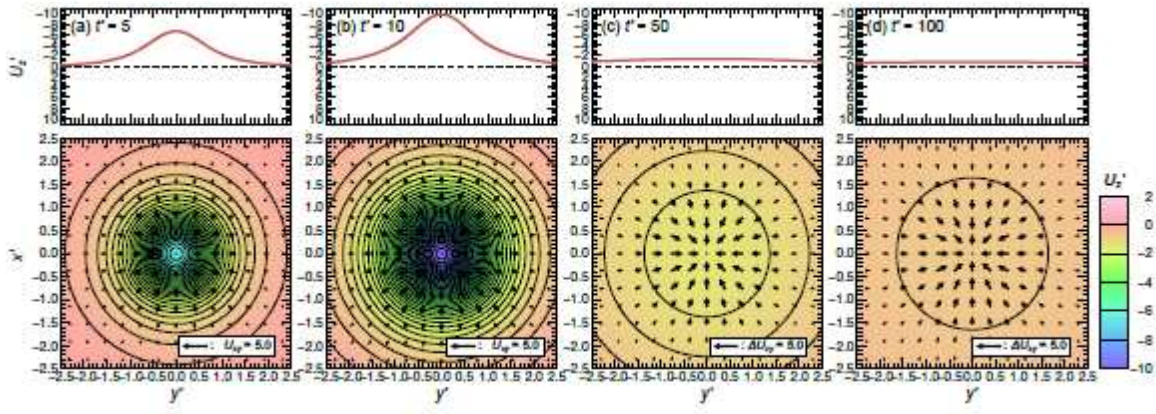


Fig. 5

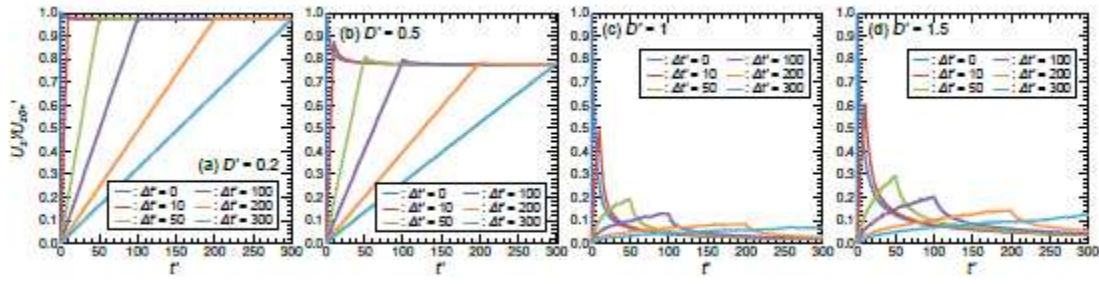


Fig. 6

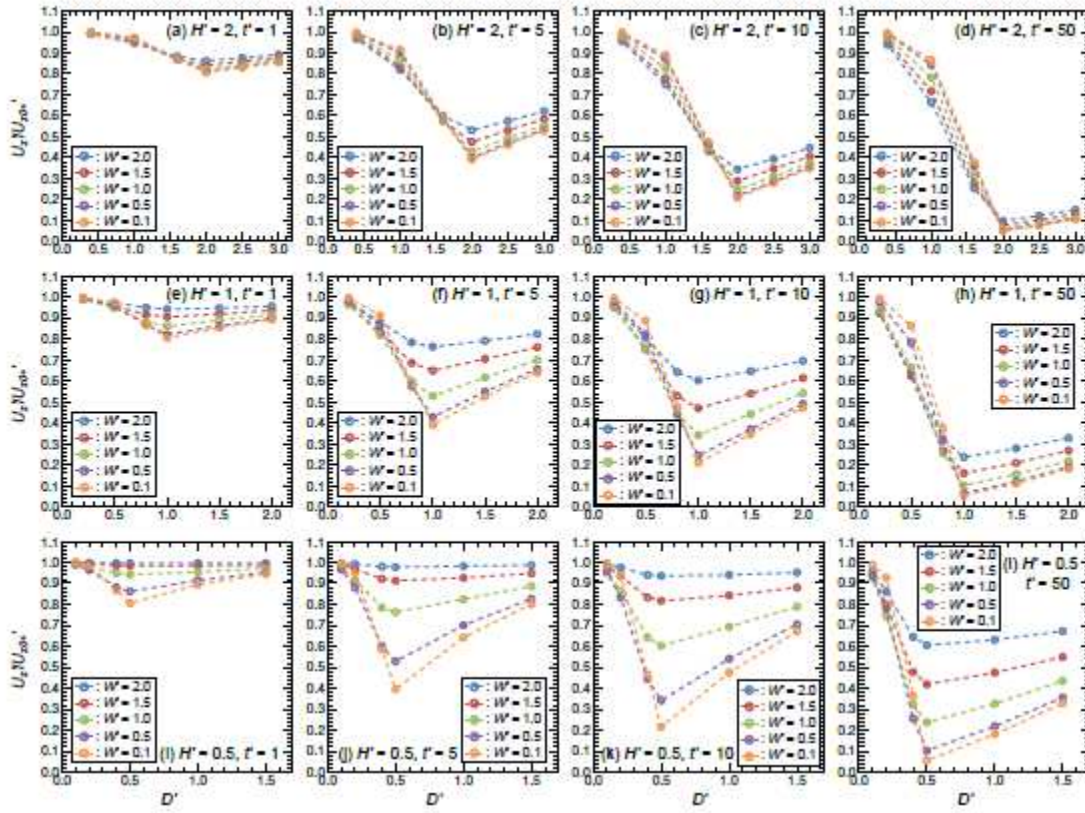


Fig. 7

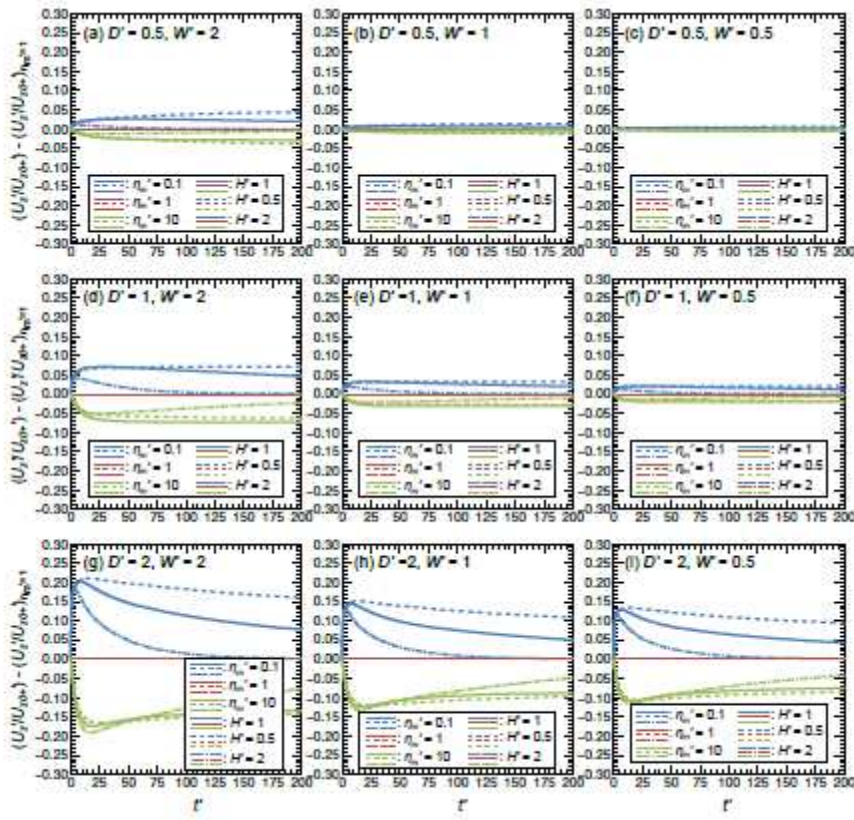


Fig. 8

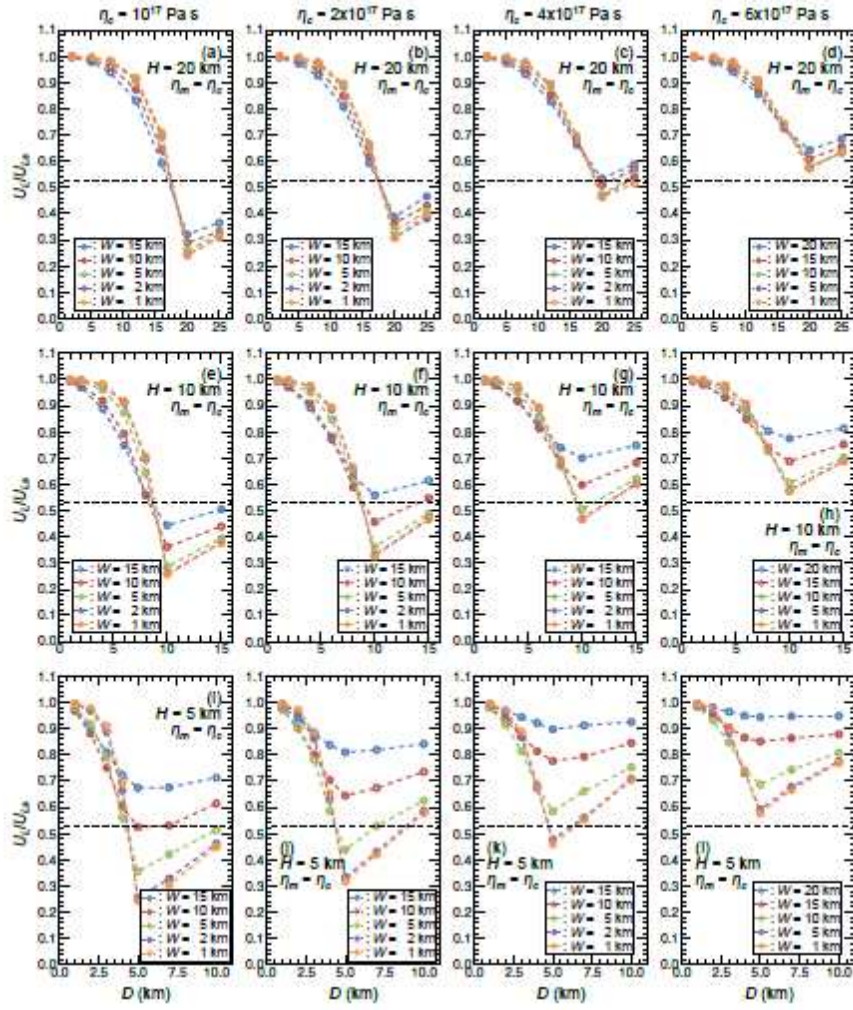


Fig. 9

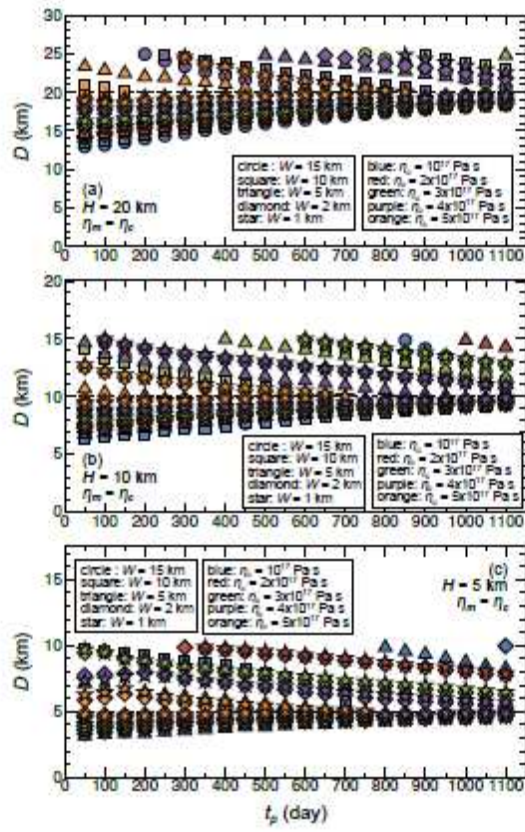


Fig. 10

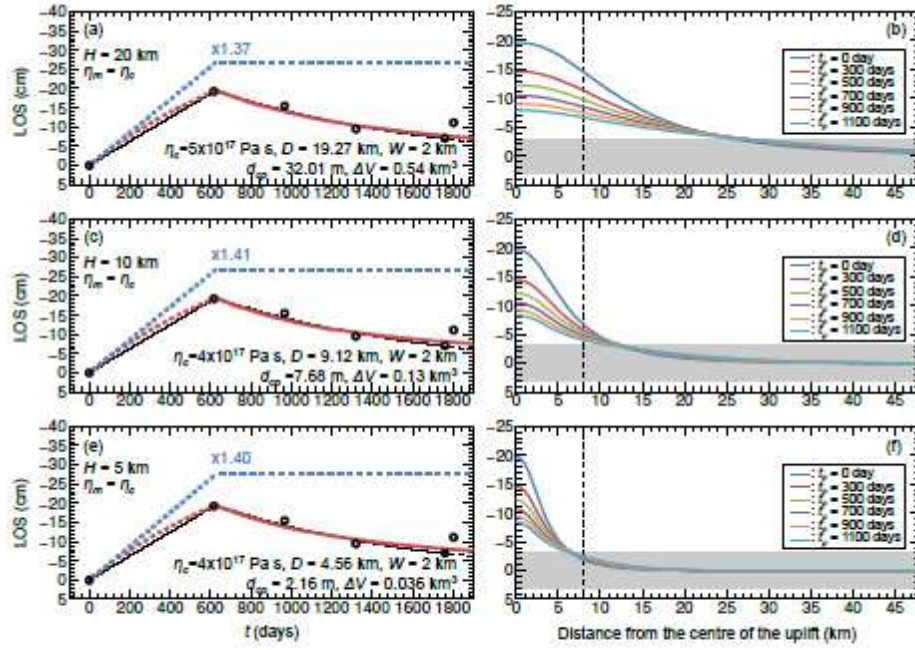


Fig. 11

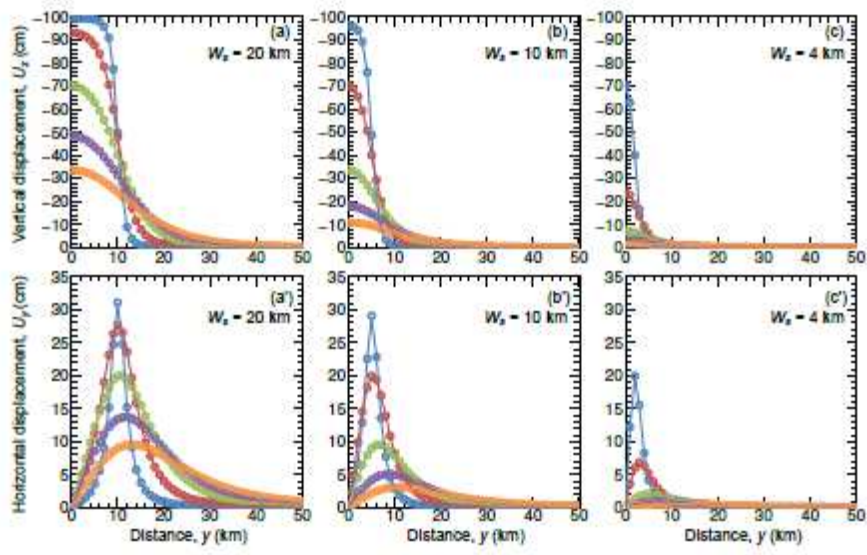


Fig. A1

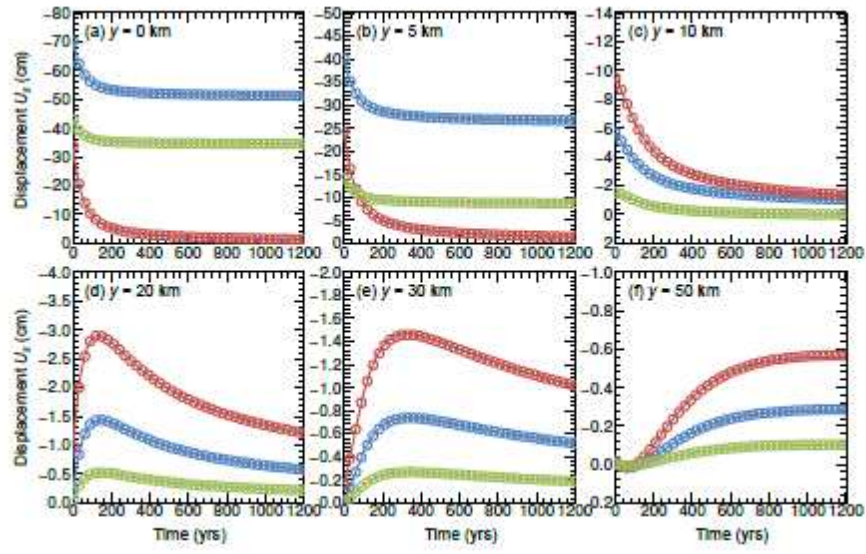


Fig. A2

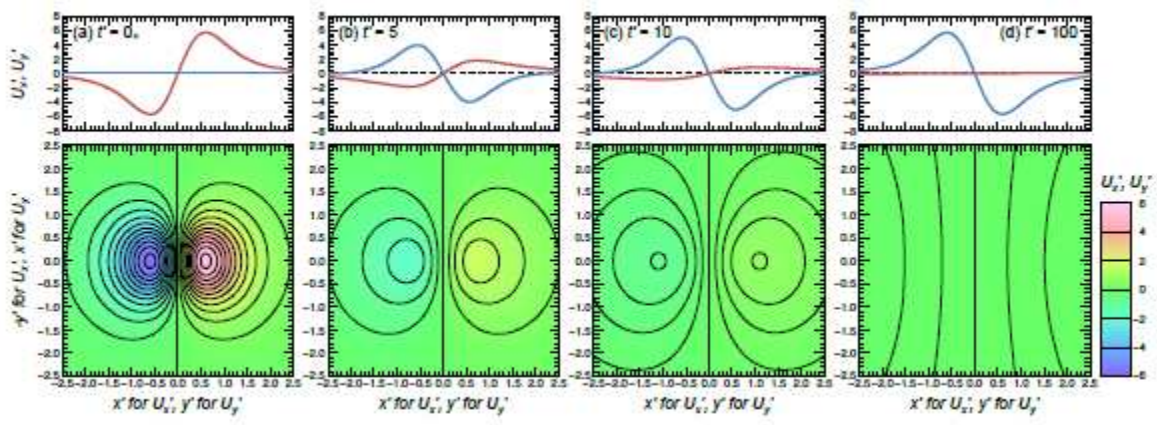


Fig. B1

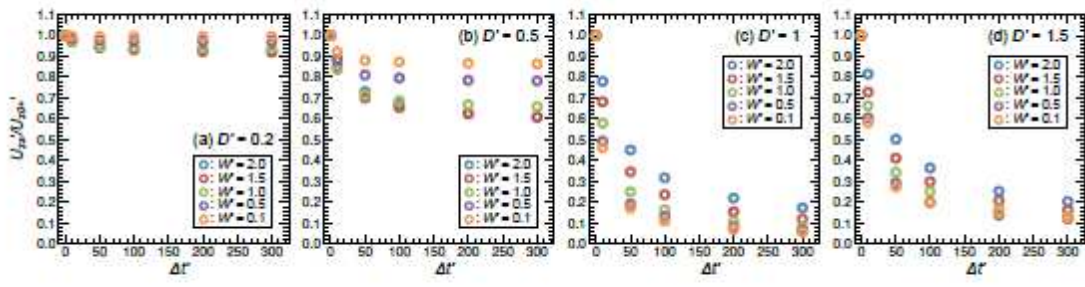


Fig. C1

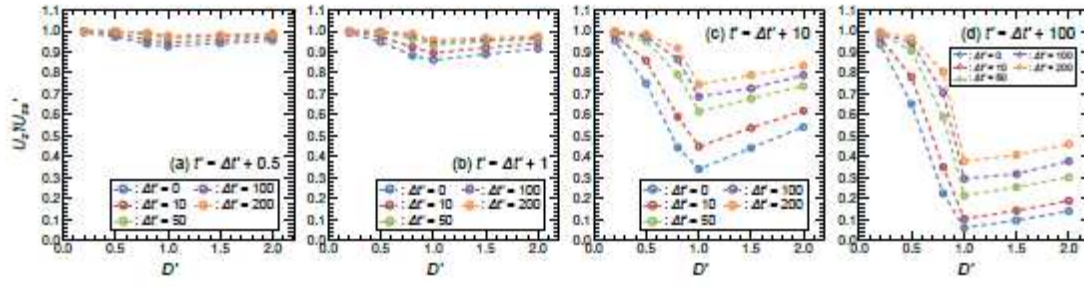


Fig. D1

Table 1: The initial elastic uplift  $U_{z0+}$  for  $\Delta t' = 0$  at  $(x', y', z) = (0, 0, 0)$ .

	$D' = 0.2$	$D' = 0.5$	$D' = 1$	$D' = 1.5$
$W' = 0.1$	-19.69	-3.88	-0.99	-0.44
$W' = 0.5$	-86.25	-50.11	-20.06	-10.03
$W' = 1$	-96.15	-80.00	-50.02	-30.79
$W' = 1.5$	-98.25	-89.99	-69.23	-50.01
$W' = 2$	-99.00	-94.11	-80.01	-64.03

 $d_{cp}' = 100$ 

ACCEPTED MANUSCRIPT

Table 2: The model parameters ( $\eta_c$ ,  $D$ , and  $W$ ) constrained from the geodetic data in different time ranges.

	$0 \leq t_p \leq 300$ days	$0 \leq t_p \leq 700$ days	$0 \leq t_p \leq 1100$ days
$(H = 20$ km)			
$\eta_c$ (Pa s)	$4 \times 10^{17}$	$5 \times 10^{17}$	$4 \times 10^{17}$
$D$ (km)	17.87	19.27	18.66
$W$ (km)	2	2	2
$(H = 10$ km)			
$\eta_c$ (Pa s)	$4 \times 10^{17}$	$4 \times 10^{17}$	$4 \times 10^{17}$
$D$ (km)	8.90	9.12	9.33
$W$ (km)	2	2	2
$(H = 5$ km)			
$\eta_c$ (Pa s)	$4 \times 10^{17}$	$4 \times 10^{17}$	$4 \times 10^{17}$
$D$ (km)	4.47	4.56	4.67
$W$ (km)	2	2	2

Table C1: The values of  $U_{zs}'/U_{z0+}'$  at  $(x', y', z', t) = (0, 0, 0, \Delta t')$ .

	$\Delta t' = 10$	$\Delta t' = 50$	$\Delta t' = 100$	$\Delta t' = 200$	$\Delta t' = 300$
$(D' = 0.2)$					
$W' = 0.1$	0.9967	0.9949	0.9945	0.9943	0.9942
$W' = 0.5$	0.9848	0.9760	0.9740	0.9728	0.9723
$W' = 1$	0.9698	0.9481	0.9427	0.9392	0.9377
$W' = 1.5$	0.9696	0.9397	0.9308	0.9245	0.9218
$W' = 2$	0.9770	0.9444	0.9325	0.9236	0.9195
$(D' = 0.5)$					
$W' = 0.1$	0.9228	0.8807	0.8720	0.8665	0.8644
$W' = 0.5$	0.8806	0.8107	0.7953	0.7857	0.7818
$W' = 1$	0.8364	0.7177	0.6877	0.6678	0.6596
$W' = 1.5$	0.8499	0.7002	0.6549	0.6229	0.6090
$W' = 2$	0.8891	0.7300	0.6715	0.6272	0.6071
$(D' = 1)$					
$W' = 0.1$	0.4634	0.1715	0.1128	0.0724	0.0580
$W' = 0.5$	0.4939	0.1932	0.1332	0.0829	0.0672
$W' = 1$	0.5791	0.2525	0.1658	0.1084	0.0842
$W' = 1.5$	0.6832	0.3476	0.2371	0.1568	0.1220
$W' = 2$	0.7804	0.4517	0.3192	0.2218	0.1736
$(D' = 1.5)$					
$W' = 0.1$	0.5820	0.2757	0.1980	0.1522	0.1251
$W' = 0.5$	0.6057	0.2941	0.2017	0.1405	0.1217
$W' = 1$	0.6633	0.3437	0.2543	0.1690	0.1323
$W' = 1.5$	0.7287	0.4124	0.2994	0.2084	0.1657
$W' = 2$	0.8151	0.5019	0.3660	0.2545	0.2058

$H' = 1.$

$U_{zs}'$  is the uplift at  $t' = \Delta t'$  for models with  $\Delta t' > 0.$

Table C2: The values of  $U_{zs}/U_{z0+}$  at  $(x', y', z', t) = (0, 0, 0, 1000)$  for  $\Delta t' = 0$ .

	$W' = 0.1$	$W' = 0.5$	$W' = 1$	$W' = 1.5$	$W' = 2$
$D' = 0.2$	0.9939	0.9710	0.9336	0.9139	0.9072
$D' = 0.5$	0.8587	0.7713	0.6365	0.5683	0.5456
$D' = 1$	0.0064	0.0079	0.0126	0.0204	0.0313
$D' = 1.5$	0.0142	0.0157	0.0204	0.0281	0.0518

$H' = 1.$

ACCEPTED MANUSCRIPT